Comparative study of deuterium retention and vacancy content of self-ion irradiated tungsten

A Hollingsworth, M.F. Barthe, M Yu Lavrentiev, P M Derlet, S L Dudarev, D R Mason, Z Hu, P Desgardin, J Hess, S Davies, et al.

Comparative study of deuterium retention and vacancy content of self-ion irradiated tungsten

A. Hollingsworth[a*], M.-F. Barthe[b], M.Yu. Lavrentiev[a], P.M. Derlet[c], S.L. Dudarev[a], D.R. Mason[a], Z. Hu[b], P. Desgardin[b], J. Hess[a], S. Davies[a], B. Thomas[a], H. Salter[a], E.F.J. Shelton[a], K. Heinola[de], K. Mizohata[d], A. De Backer[a], A. Baron-Wiechec[a,f,g], I. Jepu[h], Y. Zayachuk[a], A. Widdowson[a], E. Meslin[i], A. Morellec[i]

[a]*UK Atomic Energy Authority, CCFE, Culham Science Centre, Abingdon, Oxon, OX14 3DB, United Kingdom*
[b]*CNRS, CEMHTI UPR3079, Univ. Orléans, F-45071 Orléans, France*
[c]*Condensed Matter Theory Group, Paul Scherrer Institut, CH-5232, Villigen PSI, Switzerland*
[d]*Department of Physics, University of Helsinki, 00560 Helsinki, Finland*
[e]*International Atomic Energy Agency, A-1400, Vienna, Austria*
[f]*Technion – Israel Institute of Technology, Haifa 32000, Israel*
[g]*Guangdong Technion – Israel Institute of Technology, Shantou 515063, PR China*
[h]*Laboratory of Low Temperature Plasma, National Institute for Laser, Plasma and Radiation Physics, Magurele, Romania*
[i]*DEN-Service de Recherches de Métallurgie Physique, CEA, Université Paris-Saclay, F-91191, Gif-sur-Yvette, France*

Abstract

Self-ion irradiation of pure tungsten with 2 MeV W ions provides a way of simulating microstructures generated by neutron irradiation in tungsten components of a fusion reactor. Transmission electron microscopy (TEM) has been used to characterize defects formed in tungsten samples by ion irradiation. It was found that tungsten irradiated to 0.85 dpa at relatively low temperatures develops a characteristic microstructure dominated by dislocation loops and black dots. The density and size distribution of these defects were estimated. Some of the samples exposed to self-ion irradiation were then implanted with deuterium. Thermal Desorption Spectrometry (TDS) analysis was performed to estimate the deuterium inventory as a function of irradiation damage and deuterium release as a function of temperature. Increase of inventory with increasing irradiation dose followed by slight decrease above 0.1 dpa was found. Application of Positron Annihilation Spectroscopy (PAS) to self-irradiated but not deuterium implanted samples enabled an assessment of the density of irradiation defects as a function of exposure to high-energy ions. The PAS results show that the density of defects saturates at doses in the interval from 0.085 to 0.425 displacements per atom (dpa). These

*Corresponding author. Email: Anthony.Hollingsworth@ukaea.uk

results are discussed in the context of recent theoretical simulations exhibiting the saturation of defect microstructure in the high irradiation exposure limit. The saturation of damage found in PAS agrees with the simulation data described in the paper.

1. Introduction

Tungsten has relatively high thermal conductivity, high sputtering resistance, and mechanical strength at high temperatures. These properties have favoured its selection as the primary candidate material for the divertor of ITER [1,2], as well as a prospective material for the divertor and first wall components in DEMO [3,4]. It is expected that in ITER and DEMO tungsten will be exposed to extreme operating conditions, including direct contact with fusion plasma as well as high neutron flux. The challenges associated with the operation of tungsten components include making a quantitative characterization of the effects of the operating environment and understanding the evolution of mechanical properties as well as providing a realistic estimate of tritium retention. Retention of hydrogen and its isotopes is known to alter the physical and mechanical properties of materials, and the loss of radioactive tritium inventory is problematic both in terms of fuel efficiency and regulatory constraints [5]. Furthermore, exposure to high energy ions and neutrons gives rise to displacement cascades and production of defects in the microstructure. This requires investigating the damage that irradiation generates in tungsten, including the production of defects (vacancies and interstitials), their complexes (cavities and loops), and extended dislocation network. One of the significant questions related to the assessment of hydrogen isotope retention is the evaluation of how the density of defects, particularly vacancies, depends on the irradiation dose, since vacancies and vacancy clusters are known to act as traps for hydrogen isotopes and helium [6-8].

Deuterium retention in tungsten has been subject of numerous studies. Often, a single method of characterization has been used, such as elastic recoil detection [9], TDS [10], or nuclear reaction analysis (NRA) [11,12]. Combination of TDS and scanning electron microscopy morphology study was performed by Tyburska *et al*. [13]. Wielunska *et al*. [14] performed a combined TDS and NRA study of retention in tungsten irradiated by different ions. In this paper, we describe an experimental study of self-irradiated tungsten that uses several techniques and is supported by theoretical analysis and simulations. The study was performed within the UKAEA-led Europe-wide Tritium Retention in Controlled and Evolving Microstructure (TRiCEM) project. Some of the tungsten samples were exposed to deuterium plasma at room temperature in a new facility that enables studying the interaction of hydrogen isotopes with nuclear fusion relevant first wall materials, as well as the retention and release of

these isotopes. The new facility enables the implantation of a range of gases into the samples, including tritium. The design of this facility and the commissioning results are described in detail in a recent publication [15]. After implantation, the samples were studied using several experimental techniques, including Thermal Desorption Spectroscopy (TDS) and Transmission Electron Microscopy (TEM). Our aim is to identify peaks in the TDS spectra of irradiated tungsten, to investigate the dependence of deuterium inventory on irradiation damage, and to compare the data with earlier experimental results. Next, we performed Positron Annihilation Spectroscopy (PAS) analysis of the samples, as PAS is an established technique for the detection of vacancy-type defects [16-18]. PAS is sensitive to small defects from a single vacancy to vacancy clusters and has lower detection limit (depending on the material and the nature of the defects) in the range from about 10^{23} m^{-3} down to about 10^{20} m^{-3}, hence enabling a fairly precise determination of the density of defects.

The paper is organized as follows. In Section 2, we describe the preparation of samples used in this study, and their characterization using electron microscopy and TDS. In Section 3, we present the results of PAS analysis and give estimates for the level of damage as a function of irradiation dose. We discuss the results and their relation to recent developments in modelling and simulation of defects in materials in Section 4 and conclude in Section 5.

2. Material preparation and characterization

2.1. Preparation

Hot-rolled, 99.95% purity guaranteed pure sheet sections of tungsten were purchased from Plansee. The material was annealed in a vacuum (6×10^{-6} mbar) furnace for 20 hours at 1500°C. Circular discs of 500 µm thickness were cut using a Struers cutting saw. The samples were then polished in several stages with abrasive SiC paper form FEPA P250 to P4000 to 100 µm thickness, producing a flat surface with a thin deformation layer. Chemo-mechanical polishing using colloidal silica suspension (0.05 microns) has been used to obtain a mirror surface finish. The polished samples were then cleaned in an ultrasonic bath with iso-propanol for 15 minutes and then acetone for a further 15 minutes. Discs of 3 mm diameter were punched out from the polished specimen. Then, two types of specimen were electropolished. Specimens prepared for TEM characterisation before irradiation were double-side jet electropolished in a Tenupol-5 thinning device to produce electron-transparent thin foils. The polishing bath was composed of 2 g NaOH in 1 litre of demineralized water following Yi *et al*. [19]. Specimens prepared for

irradiation were only one-side jet electropolished for a few seconds to obtain mirror finished dimpled discs. After irradiation, the irradiated side has been protected with a varnish and TEM thin foil has been obtained by back-electropolishing using the same electrolyte as used before irradiation. The thickness of the analysed area was around 100 nm, as determined by classical thickness fringes method. Dimpled discs prepared for irradiation were shipped to the accelerator laboratory at the University of Helsinki where damage was produced by the exposure to high energy ions. Irradiation was performed using raster-scanned beam at room temperature. The ion species used for this work are 2 MeV W^+. The dependence of damage (measured in displacements per atom, dpa) as a function of depth from the surface is shown in Figure 1. It was calculated for the total fluence of 1×10^{18} ion/m^2, using two methods: the SRIM software [20-22] and the Iradina [23] codes using the Kinchin-Pease model as suggested in [21] assuming the displacement threshold energy E_d = 55 eV [24,25]. The maximum damage at around 75 nm from the surface was found to be close to 0.85 dpa. With another commonly used value of the threshold energy E_d = 90 eV, this dpa value, as well as all other damage levels given in this paper would have been reduced by about 1.6 times.

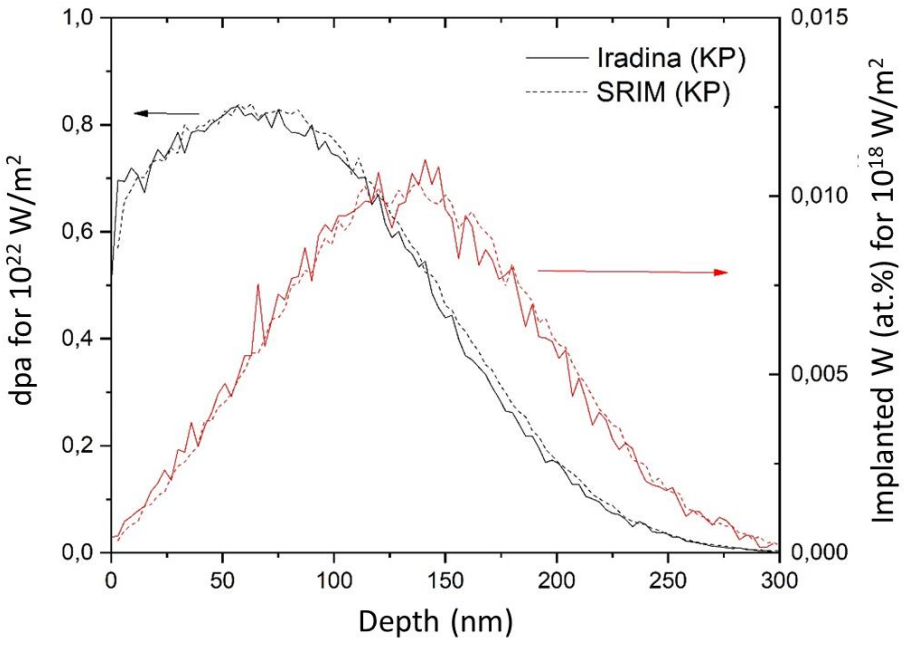

Figure 1. Damage profile (in dpa, left axis), and the density of implanted ions per unit area in the samples irradiated up to the total fluence of 1×10^{18} ion/m^2. The calculations use the Kinchin-Pease formula and were performed using the SRIM [20-22] and Iradina [23] codes, both based on the binary collision approximation [26].

The samples used in this study are described in Table 1. Deuterium implanted samples were used for TDS and TEM studies, whereas un-implanted samples were studied using Positron Annihilation Spectroscopy method.

Sample	Irradiation fluence (2 MeV W^+), atoms/m^2	Irradiation time (s)	Self-irradiation dose (dpa)	Deuterium implanted?	Characterization
S17	0	0	0	Yes	TDS
S37	0	0	0	Yes	TDS
S40	1×10^{18}	180	0.85	No	TEM
				Yes	TDS
S41	1.2×10^{17}	19	0.102	Yes	TDS
S42	1.8×10^{16}	3	0.0153	Yes	TDS
S112	0	0	0	No	PAS
S113	1×10^{16}	53	0.0085	No	PAS
S116	1×10^{17}	477	0.085	No	PAS
S119	5×10^{17}	2289	0.425	No	PAS
S123	1×10^{18}	4424	0.85	No	PAS
S125	2×10^{18}	8406	1.7	No	PAS

Table 1. List of the samples used in the current study.

2.2. Electron Microscopy

A conventional FEI 20 G2 Tecnai Transmission Electron Microscope, located at CEA Saclay and equipped with a LaB_6 source delivering 200 keV electrons, was used. Bright Field (BF) and Weak Beam Dark Field (WBDF) images were recorded to study irradiation features such as dislocation loops and lines. A camera Gatan Orius 200D has been used to record images and movies. The latter were recorded at a rate of 30 images per second.

Before irradiation, the material presented a typical annealed structure, composed of micrometric grains with low density of dislocation lines (~$10^{12}/m^2$) (Figure 2). The mean grain size, as determined by scanning electron microscopy (SEM), was about 90 µm, although much smaller grains were also present (Figure 2, right).

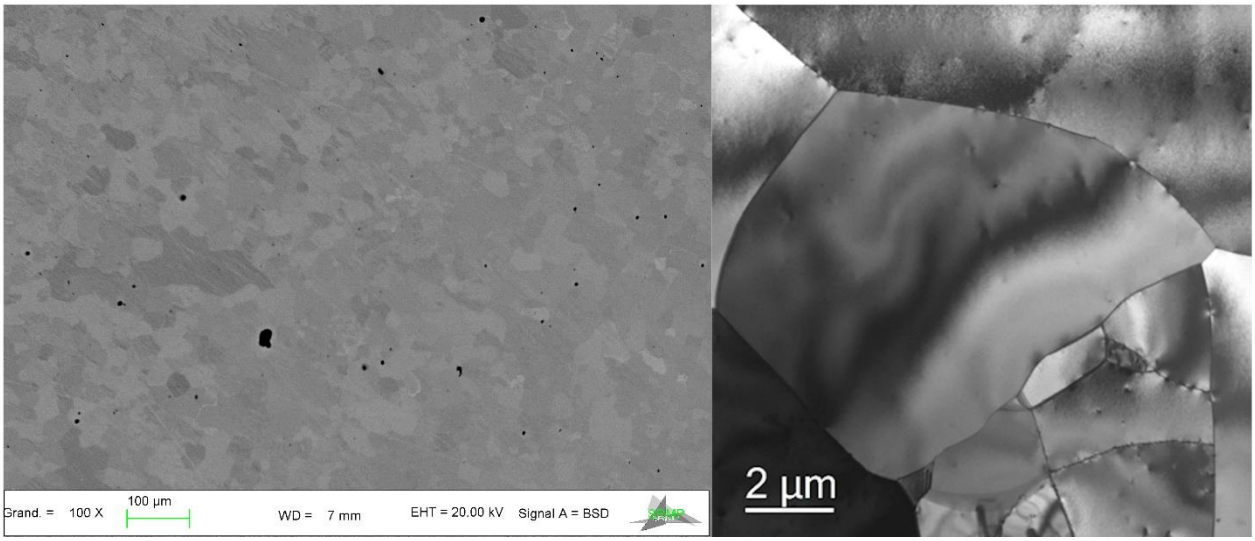

Figure 2. TEM images of electropolished tungsten before irradiation (BF image).

After irradiation, the formation of high density of irradiation defects was detected (Figure 3). They are in the form of dislocation loops and black dots. An automated analysis of the visible features seen in this region has been performed to determine the size distribution of defects. The same method as in the procedure outlined in Appendix A of [27] has been used, as shown in the Figure 4. Altogether, 1279 objects have been considered for the measurements. The mean size and volume density of defects are equal to 3.4±0.1 nm and $(3.94\pm0.1)\times10^{13}$ loops/m², respectively. A statistical error is also shown.

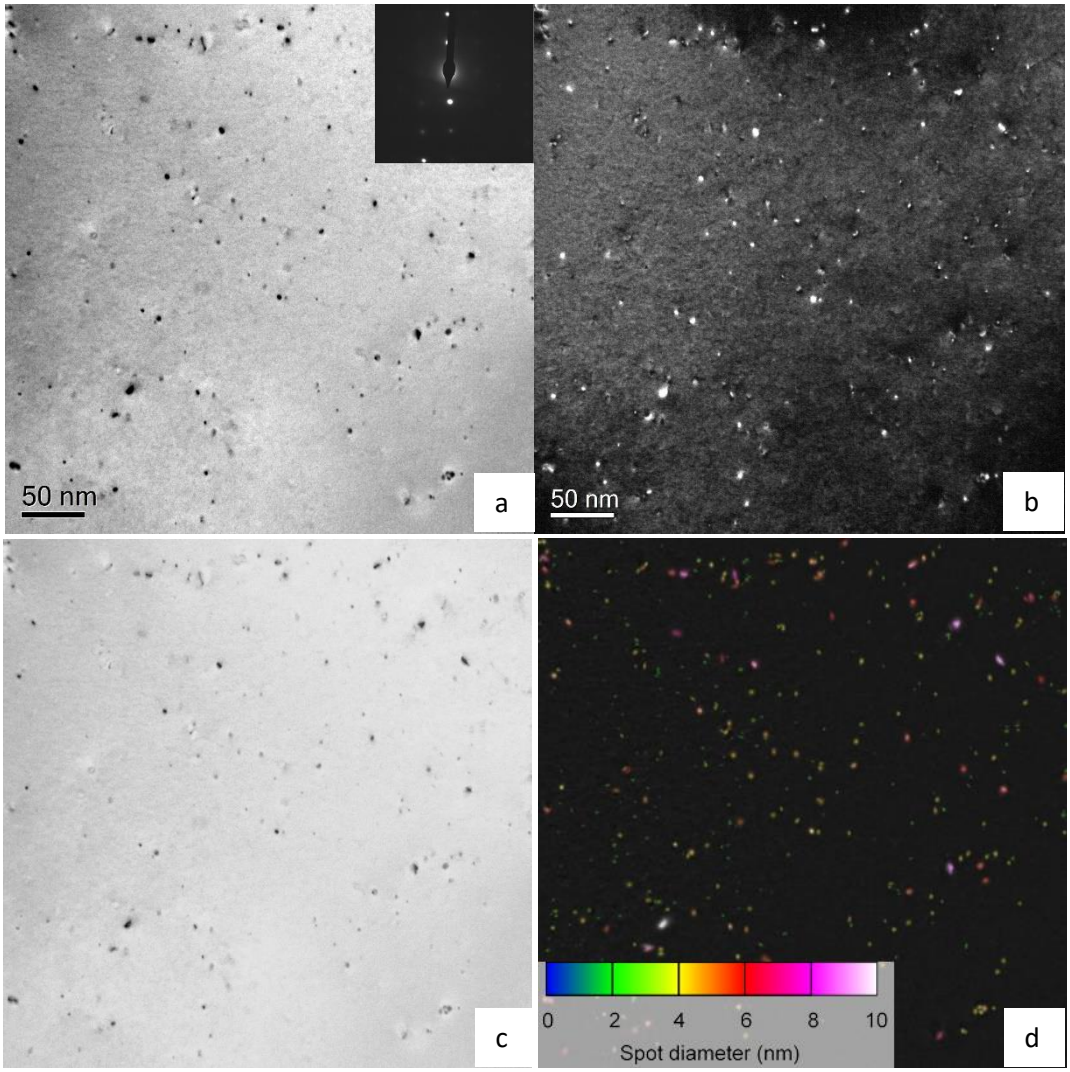

Figure 3. BF (a) and WBDF images (b) of tungsten irradiated up to 0.85 dpa at peak at room temperature. Images were performed in a <001> zone axis by using a <011> type diffracting vector. (c) and (d): the same images with the background subtracted and identified defects obtained by D. Mason's code [27].

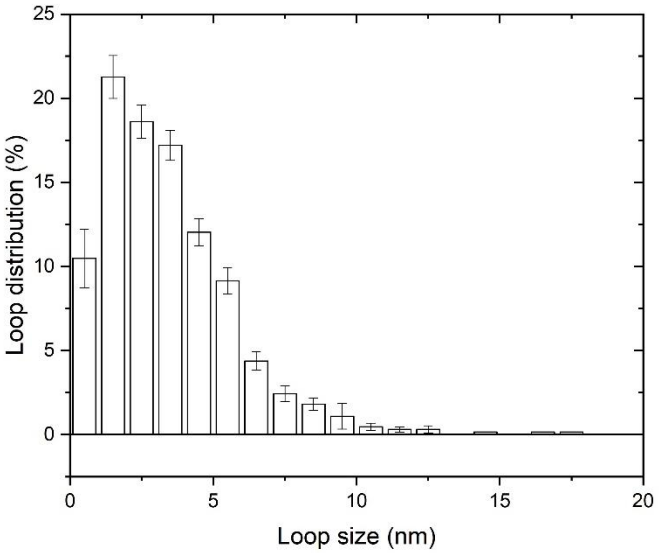

Figure 4. Size distribution of the loops formed in tungsten irradiated up to 0.85 dpa at peak at room temperature. BF images has been used to obtain the distribution.

An electron beam induced defect mobility has also been noted during the observation with 200 keV electrons at room temperature. Examples of loop jumps are given in Figure 5. Similar mobility was reported recently [28].

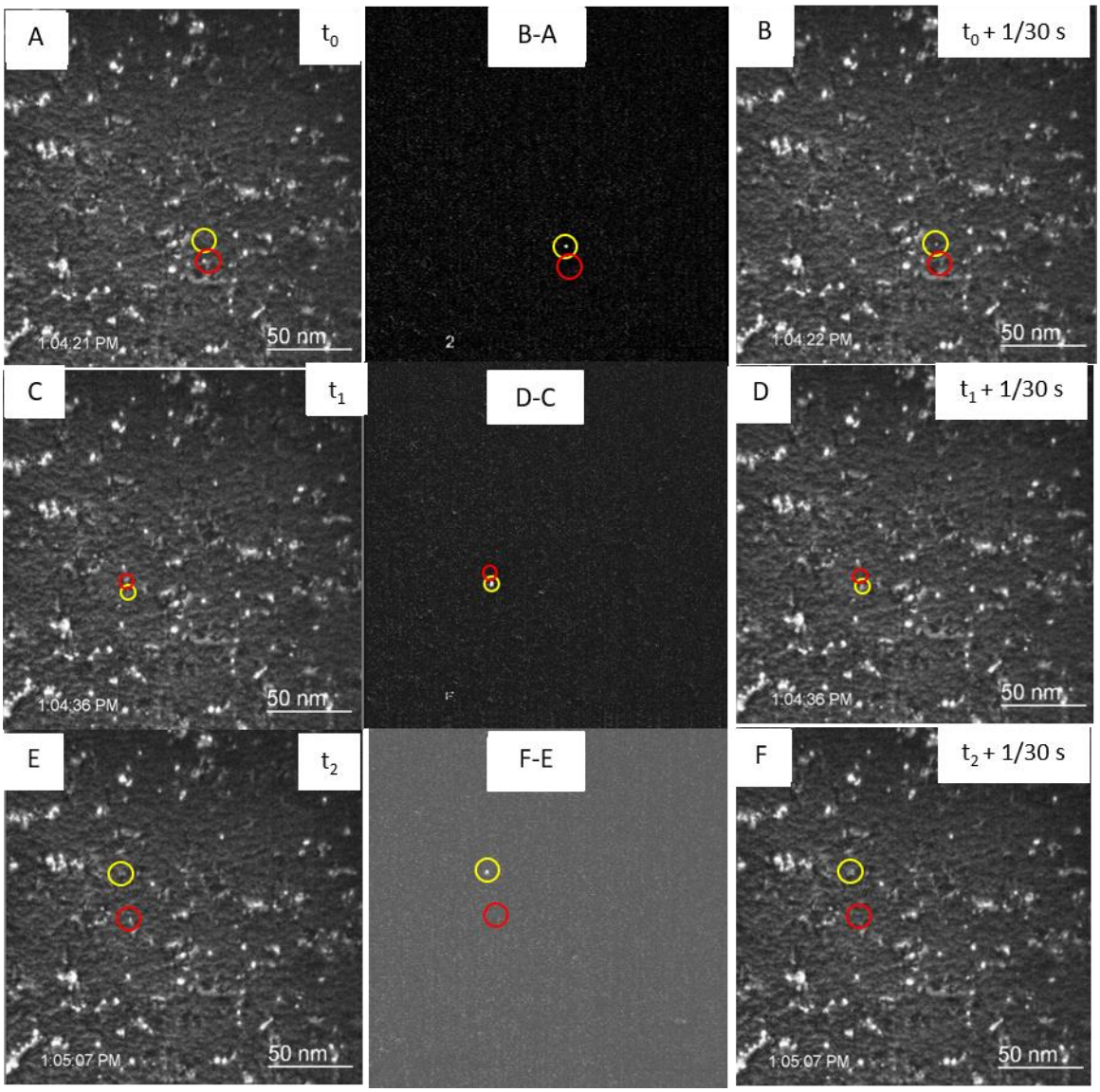

Figure 5. Three series of images extracted from the observation using 200 keV electron beam in tungsten irradiated up to 0.85 dpa at peak at room temperature (WBDF image, **z**=<001>, **g**=<110>). An example of image subtraction is shown in the middle to highlight the loop jump between A and B, C and D, and E and F frames. The initial position of the moving loop is highlighted by red circles in all the images, whereas the final position of the loop is highlighted by yellow circles.

2.3. Thermal Desorption Spectrometry

After exposure to deuterium plasma up to an estimated fluence of 10^{23} D/m^2, with ion energy 400 eV and sample's surface temperature 50 °C, TDS measurements were performed on the implanted samples using Hiden Analytical Type 640100 TPD workstation. Linear temperature ramp from room temperature to 1000°C was used, with a constant heating rate of 10 K/min. Release signals of deuterium-containing molecules – HD (mass 3) and D_2 (mass 4) were recorded using line-of-sight quadruple mass spectrometer; these were quantified using calibrated hydrogen and deuterium leaks, with calibration factor for HD signal being the average between the factors for H_2 and D_2. Total atomic deuterium release was then calculated as a sum of molecular release signals, namely $F_{atomic}(D)=F_{molecular}(HD)+2*F_{molecular}(D_2)$. The overall inventory is given in Table 2. The total deuterium retention for unirradiated samples rapidly decreases with time after the exposure, falling by almost a half after 14 days (samples S17, S37). For the irradiated samples, the total retention rises with irradiation dose up to 0.102 dpa (S41), then falls by around 20% in sample S40 irradiated to 0.85 dpa. We estimate the error of TDS inventory measurements to be ±10%, based on analysis of several identical reference samples. This alone, or combined with a difference in delay time, is not sufficient to explain the difference between the 0.102 dpa and 0.85 dpa total retention. One possible explanation for further decrease is a slight offset of the spectrum of the 0.85 dpa sample on the temperature axis compared to the other samples (Figure 6). Offsets on this axis are likely due to differences in mounting on the heating stage of the TDS. This may have led to an underestimate of the deuterium retention in the 0.85 dpa sample. On the other hand, it might be a genuine effect, deserving further study. Similar decrease of retention was found in a recent nuclear reaction analysis study of W samples irradiated to 0.5 and 5 dpa ([29], Figure 2). In any case, it is clear from the TDS results that there is no significant increase in retention between the 0.102 dpa and 0.85 dpa samples, despite an order of magnitude difference in irradiation dose. This is broadly in line with the saturation of vacancy density observed in the PAS results discussed below.

The resulting TDS spectra are shown in Figure 6. Several characteristic temperature regions can be identified, in which there are notable differences between the unirradiated and irradiated samples. The first region is a wide maximum between 350-400 K and 550-600 K, present in the spectra of all the samples. In the irradiated samples (S40-S42) the higher temperature peak

contains more deuterium, whereas in the un-irradiated samples (S17 and S37) the ratio is significantly different. The substantial decrease of the low-temperature peak in un-irradiated

Sample	Self-irradiation dose (dpa)	Delay time between deuterium exposure and TDS (days)	Total deuterium inventory ($x10^{19}$ atoms/m^2)
S17	0	1	4.693
S37	0	14	2.594
S42	0.0153	43	2.589
S41	0.102	47	4.408
S40	0.85	49	3.564

Table 2. Total deuterium inventory of the samples analysed by TDS.

sample S37 compared to S17 can be attributed to a longer delay between implantation and TDS measurements for S37, allowing the weakly bound deuterium to be released. It should be noted that the spectra of irradiated samples feature this low-temperature release stage even though the delay between D implantation and TDS measurement was significantly longer. This allows making a distinction between several kinds of traps with similar trapping energies – some of which are caused by irradiation while others are intrinsic and are present even in the unirradiated material. This maximum has been detected previously in the case of low-temperature implantation [30] and it was suggested that it might be attributed to release of deuterium from several possible weak traps, such as grain boundaries or surface adsorption sites; these are the abovementioned intrinsic defects. On the other hand, vacancies with multiple occupancy might contribute to desorption in this temperature range for irradiated samples, as it was shown that as the occupancy of traps increases, the binding energy of hydrogen isotopes decreases [7,8]. These are possible candidates for the irradiation-induced traps.

A second region is characterized by a narrow peak centered around 700-750 K, in agreement with results reported elsewhere [30-32]. This peak is present in all release spectra; however, it is evident that its magnitude significantly increases for the pre-damaged samples as compared with unirradiated ones, which indicates that this peak is associated with the defects introduced by displacement damage due to high-energy ion irradiation. The height of this peak increases with the increase of irradiation dose to 0.1 dpa. Usually, this peak is attributed to deuterium release from single vacancies. It is important to stress here the role of delay between

implantation and the TDS. In particular, the comparison of TDS spectra between two unirradiated samples: S17 (next day TDS), and S37 (TDS 14 days after exposure) shows large decrease of the 750 K peak. Even the smallest irradiation dose of 0.0153 dpa (sample S42) results in higher 750 K peak than in S37, despite even longer delay between exposure and the TDS (43 days). This confirms creation of single vacancies at very low irradiation doses.

Finally, a small broad peak was detected at around 1100 K in all the irradiated samples, with its height increasing with the increase of irradiation dose, while at the same time it is absent in the non-irradiated ones. Again, this indicates that this peak is associated with deuterium trapping on the defects associated with the displacement damage. In the literature release peak at this temperature is attributed to the release of deuterium from the gas-filled under-surface voids or vacancy clusters [33,34].

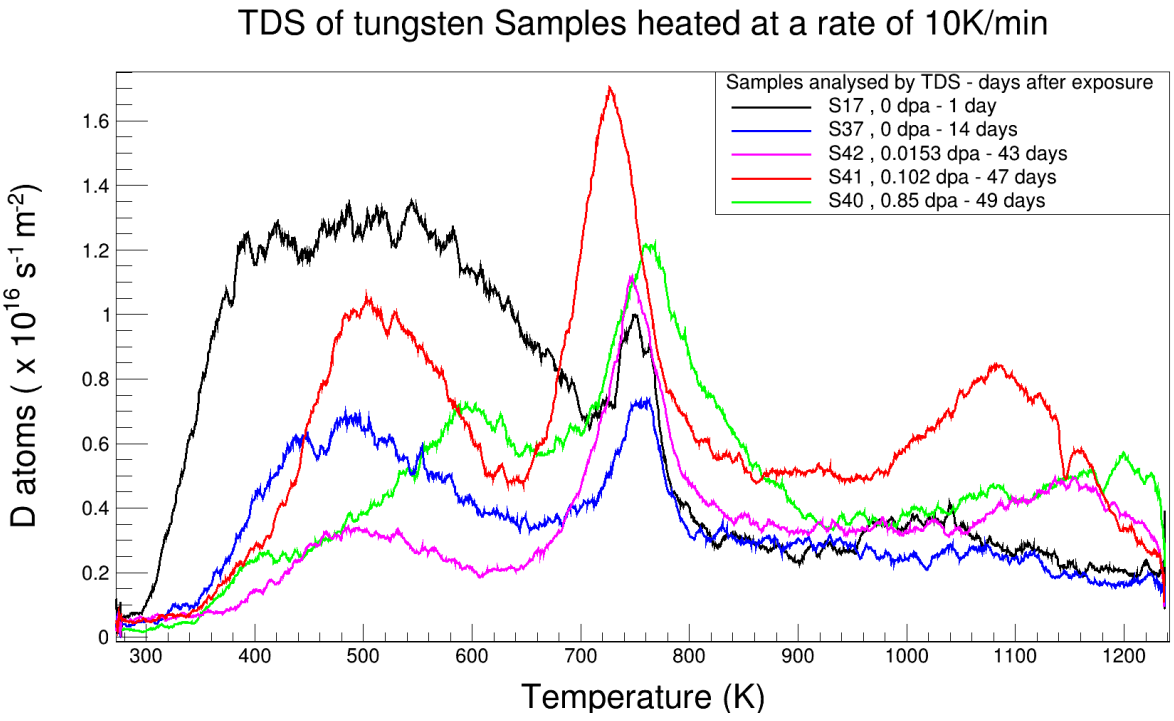

Figure 6. TDS spectra of implanted samples with damage levels between 0 and 0.85 dpa. Time period between exposure to deuterium plasma and the TDS is shown in the inset.

3. PAS Analysis

3.1. Description of the PAS system and method used

The samples were characterized by using a slow positron beam coupled to a Doppler broadening spectrometer (SPB-DB) available at the CEMHTI laboratory. A comprehensive description of the experimental setup and the basics of this powerful method are described in [35]. A monoenergetic positron beam, with a diameter of 3 mm, was generated from a ^{22}Na source. The energy of the beam was varied in the range of 0.5 to 25 keV. The spectrum of the γ-ray annihilation photons (centered at 511 keV) coming from the sample is recorded using a high-resolution gamma spectrometer equipped with a germanium detector (1.24 keV resolution at 514 keV). This Doppler broadened spectrum is characterized by two line-shape parameters: *S* and *W*. *S*, defined as the ratio of counts in the central region of the spectrum to the total counts, represents the fraction of positron-electron pairs annihilated with low momentum and is thus related mostly to annihilations with valence electrons. *W*, the ratio of counts in the wing regions of the spectrum to the total counts, represents the fraction of positron-electron pairs annihilated with high momentum and hence is more specifically related to the annihilations of positrons with core electrons. For our experiments, the momentum ranges for the calculation of *S* and *W* are 0-$\left|2.80\right|\times10^{-3}\ m_e c$ and $\left|10.61\right|\times10^{-3}$ - $\left|26.35\right|\times10^{-3}\ m_e c$, respectively, where m_e is the electron mass and *c* the speed of light. These momentum ranges correspond to ranges of energies of photons emitted as a result of annihilation of 510.28 – 511.72 keV for the *S* photons, and 504.27 – 508.29 keV and 513.71 – 517.73 keV for the *W* photons. Each material exhibits specific S_L and W_L values, as a signature of the momentum distribution of electrons in the perfect lattice in the absence of vacancy defects. The sensitivity of the PAS technique to the type and concentration of vacancy defects in solids is based on the fact that positrons are more susceptible to being trapped at open volume defects where the electron density is low, before annihilation [16]. When positrons are trapped at vacancies, their smaller overlap with core electrons narrows the positron-electron momentum distribution, resulting in an increase of *S* and decrease of *W*. Hence *S* and *W* yield information about the presence of vacancy defects in solids as parameter *S* increases and *W* decreases. Each type of vacancy cluster *j* is characterized by some specific values of S_j and W_j. Generally, *S* increases and *W* decreases when the number of vacancies *n* in the cluster V_n increases.

For this study, *S(E)* and *W(E)* were recorded as functions of positron energy *E* spanning the range from 0.5 to 25 keV. This energy range corresponds to the mean positron implantation

depth in tungsten between approximately 0.4 and 300 nm. Note that the full-width-at-half-maximum of the implanted positrons distribution increases with the energy, to reach ≈ 380 nm at 25 keV. At this energy, positrons probe up to ≈ 700 nm depth below the tungsten surface, i.e. all the damaged region, as can be seen in Figure 7. The *S* value measured at energy *E* depends on the defect distribution and diffusion properties of the positrons in the sample. A modified version of VEPFIT program [36] allows the calculation of *S(E)* and *W(E)* taking into account positrons implantation and their diffusion, assuming that the defect depth profile is a sequence of homogeneous layers. Note that the diffusion of positrons is limited by their trapping at defects and hence the effective diffusion length that L_{eff}^{+} can be written as follows [37]:

$$L_{eff}^{+} = \sqrt{\frac{D^{+}}{\lambda_L + \sum_{j=1}^{m} K_j}} \quad (1)$$

where K_j are the positron trapping rates at various detected defects (single vacancy, vacancy clusters V_n, dislocations etc.), D^+ is the intrinsic positron diffusion coefficient ($D^+ = 1.26\times10^{-4}$ m^2/s for tungsten [38]), and λ_L the lattice annihilation rate ($\lambda_L = 1/\tau_L$, τ_L= 101-105 ps [39,40]). Hereafter, VEPFIT is used for consistently fitting the *S(E)* and *W(E)* curves allowing the extraction of the *S(z)* and *W(z)* depth profiles and the effective diffusion length in each layer. Note that the data for the positron energy below 2.0 keV were discarded because for this low energy, the positron's migration does not result, in the present case, in a diffusion process.

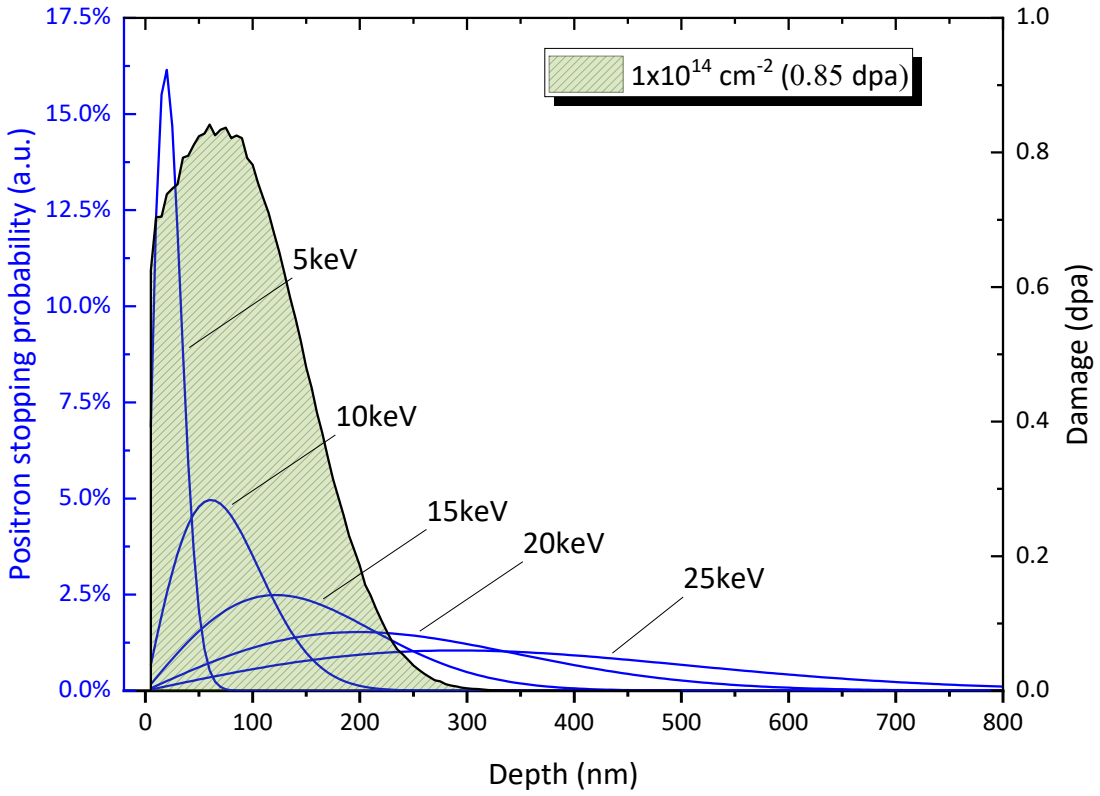

Figure 7. Implantation profiles of 5, 10, 15, 20 and 25 keV positrons in tungsten compared to the SRIM calculations of the damage profile of 2 MeV W^+ ions implanted at a 1×10^{14} atoms/cm^2 fluence at room temperature, taking a displacement threshold energy of 55 eV [24,25] in the Kinchin-Pease model as recommended by Stoller *et al.* [21].

The line-shape parameter $S(z)$ (or in the case where the vacancy defect depth profile is modelled as a succession of homogeneous layers, $S_{lay}(i)$ corresponding to the S value in layer i) is related to the specific values S_j of the trapping defects j at which positrons are annihilating and the fraction of annihilation of these defects f_j as given in equation (2) below. Also, $W(z)$ (or $W_{lay}(i)$) can be expressed in the same way:

$$S_{lay}(i) = f_L \times S_L + \sum_{j=1}^{m} S_j \times f_j, \qquad W_{lay}(i) = f_L \times W_L + \sum_{j=1}^{m} W_j \times f_j, \qquad (2)$$

where the specific annihilation fractions f_L for annihilation in the lattice and f_j for the case of positron trapping at traps j from which no detrapping can occur because the trapping energy at these traps is high enough for the measurement temperature [10], can be written as follows:

$$f_L = \frac{\lambda_L}{(\lambda_L + \sum_{j=1}^{m} K_j)}, \qquad f_j = \frac{K_j}{(\lambda_L + \sum_{j=1}^{m} K_j)} \qquad (3)$$

$S_{lay}(i)$ and $W_{lay}(i)$ values are related to the total positron trapping rate K_j at the detected defects j. K_j is the product of the traps concentration C_j by their specific trapping coefficient μ_j. The

specific trapping coefficient μ_V of single vacancy in tungsten is approximated to the value determined for the single vacancy in Ta which has Z value close to tungsten ($\mu_V = 6 \pm 3 \times 10^{-9}$ cm^3/s [16]). It is expected that the specific trapping coefficient for vacancy clusters V_n is n times the trapping coefficient of a single vacancy ($\mu_{Vn} = n \times \mu_V$) when n is lower than 10 [16].

Some annihilation characteristics have been already experimentally determined in tungsten. For the perfect lattice, the annihilation characteristics are $S_L = 0.367(4)$ and $W_L = 0.084(5)$; for the single vacancy, $S_V = 0.417(1)$ and $W_V = 0.057(1)$ [41,42]. The $\left| (S_V - S_L)/(W_V - W_L) \right|$ ratio is equal to 1.85(3) and can be assigned to annihilation of positrons as trapped at single vacancy. The annihilation characteristics S_{Vn}, W_{Vn} of vacancy clusters are not known, only for some V_n positron lifetimes (τ_{Vn}) have been already calculated [39]. τ_{Vn} increases with n, meaning that it increases as a function of the size of a vacancy cluster. τ_{Vn} becomes constant when n is so high that the positron annihilates close to the surface of the cluster, as the electron density is negligible inside the vacancy cluster. Saturation occurs when n becomes larger than 20 vacancies [39]. The maximum and minimum values of line-shape parameters were obtained in earlier studies that we carried out in tungsten and are as follows: $S_{Max} = 0.5026$, $W_{Min} = 0.0364$. S_{Max} and W_{Min} are most probably related to the annihilation in vacancy clusters with the maximum size detectable with SPB-DB that means V_N where N is equal or larger than 20 as it has been also observed for the positron lifetime in the theoretical study from [39]. The $\left| (S_{max} - S_L)/(W_{min} - W_L) \right|$ ratio (equal to 2.8) can be assigned to annihilation in vacancy cluster V_N where N is equal or larger than 20 vacancies.

Note that positrons can be also trapped at <100> edge and ½ <111> screw dislocations as it has been calculated for iron and tungsten [43] and observed in iron [44] and in tungsten [45]. The specific annihilation characteristics S_j, W_j of this type of defects have not yet been determined in tungsten. Only the calculated positron lifetimes can be found in literature [43,46]. Depending on the nature of a dislocation, the lifetime varies generally between a value close to the lifetime in the perfect lattice (τ_L =101 ps in tungsten) [39] and the one in a single vacancy (τ_V =193 ps in tungsten) [35] due to the fact that open volume is lower in the core of a dislocation than in a vacancy. The positron lifetime in the core of ½ <111> screw and <100> edge dislocations has been calculated as 130 ps and 161 ps, respectively [43]. When vacancies are bound to the dislocation line, the lifetime increases and reaches a value close to the lifetime of a positron in a bound vacancy cluster. The same trends have been found in iron [43]. Recently the values of S_{dis} and W_{dis} specific to dislocations have been determined for iron [47]. As expected, the characteristic $\left| (S_{dis} - S_L)/(W_{dis} - W_L) \right|$ ratio is lower than the same ratio for a single

vacancy V $\left|(S_V\text{-}S_L)/(W_V\text{-}W_L)\right|$. The same relationship is also expected for the bcc tungsten. The trapping coefficient of positrons at a dislocation μ_{disl} is not known for tungsten.

3.2 Unirradiated samples results

The *S(E)* and *W(E)* curves measured in unirradiated tungsten sample are plotted in Figure 8. These experimental data can be fitted with the VEPFIT program, considering the sample as one homogeneous layer. The results are reported in Table 3. The line-shape parameters for unirradiated sample are S_{unirr} = 0.370(1), W_{unirr} = 0.083(1). These values are respectively slightly higher and lower than the perfect lattice parameters S_L and W_L. This indicates that some of the positrons annihilate while trapped in vacancy defects, but the concentration of these defects remains low. This is also confirmed by the high value of the effective diffusion length of 80±1 nm which appears to be very close to the values available in literature for perfect crystalline tungsten [37,41], namely 80–135 nm. This indicates that the concentration of defects in the bulk of un-irradiated sample is low, and lower than 10^{24} m^{-3}.

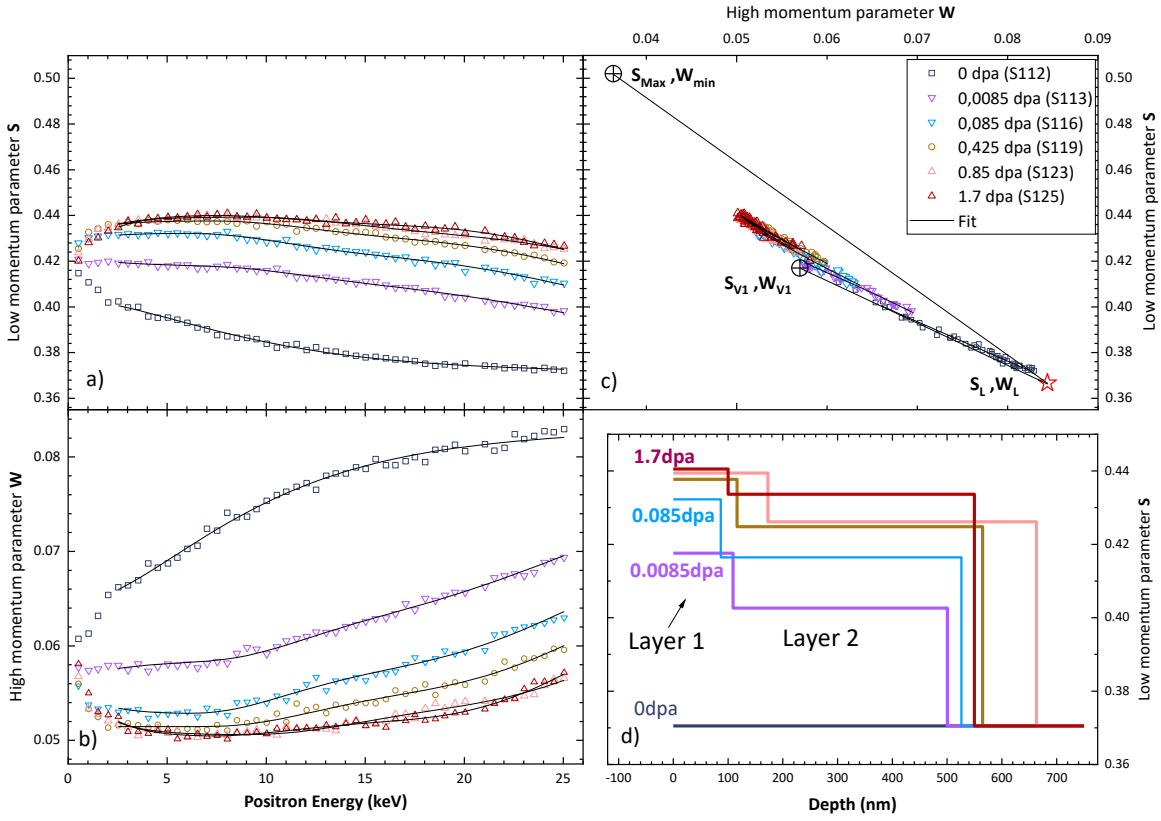

Figure 8. Evolution of the positron annihilation characteristics in unirradiated tungsten sample and in samples after irradiation to doses between 0.0085 and 1.7 dpa. (a) Low momentum fraction *S*, and (b) high momentum fraction *W* as functions of the positron energy. (c) *W* plotted as a function of *S*. The *S*, *W* values for the annihilation in lattice (S_L, W_L), single vacancy (S_{V1}, W_{V1}), and maximum *S* and minimum *W* are also plotted (S_{Max}, W_{Max}). The experimental data

are plotted in open symbols and the fitted curves are given in continuous line. (d) the *S(z)* and *W(z)* depth profiles extracted from *S(E)* and *W(E)* using VEPFIT (see details in the text).

3.3. Irradiated samples results

Line-shape parameters *S(E)* and *W(E)* measured after irradiation with 2 MeV tungsten ions at various fluences are plotted in Figure 8. With increasing irradiation dose, the *S* and *W* values drastically increase and decrease, respectively. This indicates that positrons respond to the presence of defects generated during implantation for all the fluences studied.

For the sample irradiated at the lowest dpa level (0.0085 dpa), *S* remains constant in the energy range between 0.5 and 8 keV and then decreases slowly. This indicates that the damage level decreases when the depth increases, in agreement with SRIM calculations. The $|(S-S_L)/(W-W_L)|$ ratio for the plateau values (1.96(4)) is higher than the one for the single vacancy (1.85(3)) indicating that vacancy clusters are detected. These clusters are probably formed in collision cascades. Fitting of *S(E)* and *W(E)* with the VEPFIT program requires a model with a minimum of 3 homogeneous layers to correctly describe the experimental curves. Models with 3 and 4 layers have been tested. The one with 3 layers has been chosen because the number of parameters is minimized, and the quality of the fit is acceptable (as seen in Figure 8). In these fits the annihilation characteristics of the last layer, which is not damaged, have been fixed at values $S_{Lay}(3)$ = 0.370, $W_{Lay}(3)$ = 0.083 and the effective diffusion length $L_{Lay}(3)$ was taken to be 80 nm in agreement with the values obtained for the bulk of unirradiated samples. The annihilation characteristics extracted for layers 1 and 2, S_{Lay}, W_{Lay}, and L_{Lay} are reported in Table 3 with the annihilation characteristics S_{Surf} and W_{Surf} at the surface of the samples. The thickness of the first layer is about 100 nm for the irradiated samples with damage dose lower or equal to 0.425 dpa. This value is close to the depth of maximal damage at the maximum dpa level calculated using SRIM (see Figure 7). When the dpa level becomes equal or larger than 0.85 dpa, the thickness of the first layer increases to about 170 nm. The $S_{Lay}(1)$, $W_{Lay}(1)$ values extracted from the fitting correspond to the maximum damage induced for each damage dose. Note that these values represent the mean of *S(E)* and *W(E)* calculated in the energy range between 7 and 8.5 keV.

		Damage dose (dpa)				
		0.0085	0.085	0.425	0.85	1.7
	S_{Surf}	0.419(1)	0.430(1)	0.432(1)	0.431(1)	0.431(1)

Surface	W_{Surf}	0.057(1)	0.054(1)	0.053(1)	0.054(1)	0.054(1)
Layer 1	S_{Lay}	0.418(1)	0.432(1)	0.438(1)	0.440(1)	0.440(1)
	W_{Lay}	0.058(1)	0.053(1)	0.051(1)	0.050(1)	0.050(1)
	$(S_{Lay}\_S_L)/(W_{Lay}-W_L)$	1.96(4)	2.10(4)	2.15(4)	2.15(4)	2.15(4)
	$L^+_{Lay\ (nm)}$	14(4)	4-6	4-5	5-7	5-7
	Thickness (nm)	100(5)	90(5)	110(10)	120-170	120-170
Layer 2	S_{Lay}	0.402(1)	0.417(1)	0.425(1)	0.428(5)	0.428(5)
	W_{Lay}	0.067(1)	0.059(1)	0.057(1)	0.054(2)	0.054(2)
	$L^+_{Lay\ (nm)}$	60	50	45	30	30
	Thickness (nm)	510(10)	510(20)	570(10)	610(45)	610(45)
Vacancy concentration (m^{-3})		9.2×10^{25}				
Mean defect size by TEM (nm)					3.4±0.1	
Mean defect volume density by TEM (loops/m^2)					$(3.94\pm0.1)\times10^{13}$	

Table 3. Annihilation characteristics S_{Surf} *and* S_{Surf} for surface, $S_{Lay}(i)$, $W_{Lay}(i)$**,** and $L_{Lay}(i)$ for layers i = 1,2, extracted from fitting of the *S(E)* and *W(E)* curves with the VEPFIT program using a three layers model for irradiated samples at different damage doses between 0.0085 and 1.7 dpa.

$S_{Lay}(1)$ increases and $W_{Lay}(1)$ decreases first rapidly when damage dose reaches 0.085 dpa and then more slowly to 0.85 dpa. Then, they remain constant when damage dose is increased again by a factor of 2. The saturation values of $S_{Lay}(1)$ and $W_{Lay}(1)$ are $S_{Sat}(1)$ = 0.440(1) and $W_{Sat}(1)$ = 0.050(1). Note that they are the same as the values obtained for damage dose of 1 dpa and also 12 dpa using other irradiation conditions (20 MeV W^+ ions at room temperature [48]). The $S_{Lay}(1)/S_L$ normalized values measured in the irradiated samples are plotted as a function of dpa level in Figure 9.

The effective diffusion length L_{Lay} (1), is 14(4) nm after irradiation at the lowest damage dose. It is much lower than in the virgin sample (80(1) nm) indicating a high positrons trapping rate at defects. L_{Lay} (1) decreases to a very low value of 4-6 nm when irradiation fluence increases indicating that the concentration of defects increases. Finally, L_{Lay} (1) remains constant for high damage dose equal or higher than 0.085 dpa.

The $\left|(S_{Lay}(1)-S_L)/(W_{Lay}(1)-W_L)\right|$ ratio also increases slightly when the dose increases up to 0.425 dpa, indicating that the proportion of the largest vacancy clusters increases with the damage dose probably because of the overlap of collision cascades. As the values of $S_{Lay}(1)$ and $W_{Lay}(1)$ and L_{Lay} (1), this ratio doesn't change for the highest damage doses larger or equal

than 0.85 dpa. Overall, PAS results detect a saturation when the dpa level becomes higher than 0.425 dpa indicating that the types of vacancy defects detected no more change. Such saturation can be due to either the saturation of the induced damage or to the saturation of positron trapping at the detected type of defects and no change in the annihilation characteristics can be observed. This point will be discussed in Section 4. Similar saturation in tungsten has been observed by Ogorodnikova and Gann [49] when studying deuterium concentration after irradiation with 20 MeV W ions, with saturation dose of ~0.45 dpa, very close to 0.425 dpa in the present study. The effect of saturation was also found in Eurofer steel at 0.25 dpa [50], while another study [15] found rapid saturation (below 0.1 dpa) in Fe-Cr alloy but decrease of overall deuterium concentration in Eurofer at 1 dpa compared to 0.1 dpa. It can be added that if the concentration of defects would increase with damage dose the PAS results show that the proportion of the different defects does not change.

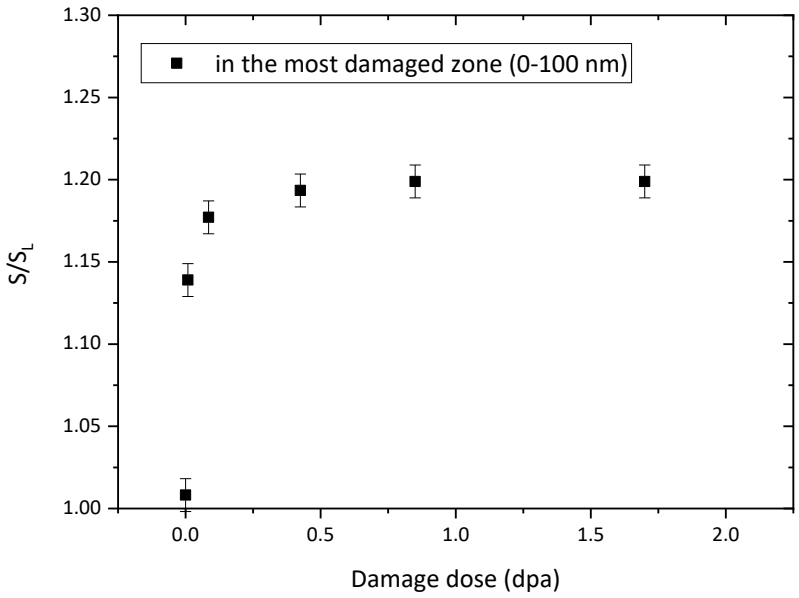

Figure 9. Low momentum annihilation fraction in the most damaged zone as a function of dpa level in self irradiated (2 MeV W^+ ions) tungsten samples.

4. Discussion

We have seen above that the *S* and *W* values obtained in the most damaged zone of self-irradiated tungsten samples vary with damage dose. The *S*, *W* values in the sample irradiated

at the lowest damage dose (0.0085 dpa) are very close to the annihilation characteristics of a single vacancy suggesting that single vacancies represent the majority of vacancy type defects. The concentration of these individual vacancies C_V can be estimated from the effective diffusion length using a one trap trapping model where positrons can annihilate in only one type of defect, a single vacancy. C_V can be extracted from (1) where K_j with $j > 1$ is equal to 0 as it has been done already for Ni containing a high concentration of defects [51]. Thus C_V can be written as follows:

$$C_V = {\lambda_L}/{\mu_V}\left[\left({L^+}/{L_{eff}^+}\right)^2 - 1\right] \quad (4)$$

where L_{eff}^+ is the effective diffusion length in the damaged layer, L^+ is the intrinsic positron diffusion length (80-135 nm), λ_L the lattice annihilation rate ($\lambda_L = 1/\tau_L$), and μ_V the trapping coefficient of a positron at a single vacancy.

For the lowest damage dose, L_{eff}^+ has been found to be equal to 14(4) nm (see Table 3) and the corresponding vacancy concentration has the mean value of 9.2×10^{25} m^{-3}. As the damage dose increases, we observe that L_{eff}^+ decreases and that the $\left|(S_{Lay}(1)-S_L)/(W_{Lay}(1)-W_L)\right|$ ratio increases, indicating that positron trapping increases and that vacancy clusters are detected. The one trap trapping model can no longer be used, and the values of *S* and *W* become the results of annihilation of positrons trapped in a variety of vacancy defects, single vacancies, vacancy clusters and possibly at some dislocation type defects. TEM results presented in Section 2.2 showed that dislocation loops are generated in self-irradiated samples as it was already observed in literature (see [52], for example). Their density per unit area is estimated to be $(3.94\pm0.1)\times10^{13}$ loops/m² at 0.85 dpa. If we consider that the thickness of the sample is in the range from 50 to 150 nm (to ensure that the sample is transparent to 200 keV electrons) the loops volume density can be estimated to be in the range from $3\text{-}8\times10^{20}$ m^{-3}. We note that this density was evaluated using only one diffraction vector **g** =<110>. If we assume that both families of <100> and ½ <111> loops are generated in the same proportion during irradiation, we estimate from the invisibility rules that only 60% of the dislocation loops are detected. As showed in [45], the fraction of the <100> loops is expected to be lower than the ½<111> loops. If we consider, as the worst-case scenario, that no <100> loops are created, only 50% of loops are detected in the observation conditions used in this study. Even if we take into account that not all the dislocation loops are detected, their concentration remains low and at most can be twice the one measured in TEM micrographs, meaning that it is in the range from $0.6\text{-}1.6\times10^{21}$

m^{-3} for 0.85 dpa. At this damage dose the fraction of positrons that could be trapped at dislocation loops is negligible and positron annihilation characteristics are only representative of vacancy defects, including single vacancies and vacancy clusters V_n.

The value of the $|(S_{Lay}(1)-S_L)/(W_{Lay}(1)-W_L)|$ ratio in the damaged layer reaches 2.15 at the maximum when the damage dose becomes equal or higher than 0.425 dpa. This value corresponds to an intermediate value between the V_N related ratio ($|(S_{max}-S_L)/(W_{min}-W_L)| = 2.8$) and the single vacancy one ($|(S_V-S_L)/(W_V-W_L)| = 1.8$). It suggests that vacancy clusters V_n detected in the damaged layer are small and n is probably not larger than 5-7. When the dose becomes larger than 0.0085 dpa, positrons annihilate in single vacancy defects and in vacancy clusters V_n where n varies from 2 to 5-7. The concentration of each type of defect cannot be determined because not only are the specific values S_{Vn}, W_{Vn} of vacancy clusters V_n are not known but also because their corresponding annihilation fractions cannot be extracted. Nevertheless the total positron trapping rate K_{tot} can be written as the sum of the trapping rate in single vacancies and the trapping rate in each type of vacancy clusters: $K_{tot} = K_V + \sum_{n=2}^{5-7} K_{V_n}$. The concentration of each type of defect cannot be determined because not only are the S_{Vi}, W_{Vi} of vacancy clusters not known, but also because their corresponding annihilation fractions cannot be extracted. It is however possible to extract from the effective diffusion length L_{eff}^{+} obtained in the damaged layer the total vacancy defects concentration. Indeed, L_{eff}^{+} can be written as follows:

$$L_{eff}^{+} = \sqrt{\frac{D_+}{\lambda_L + K_V + \sum_{N=2}^{5-7} K_{V_n}}} \quad (5)$$

where K_V and K_{V_n} are the positron trapping rates at the single vacancy and the vacancy clusters V_n, respectively. For L_{eff}^{+} = 4 nm (see Table 3), $K_V + \sum_{N=2}^{5-7} K_{V_n} = 7.2\times10^{12}$ s^{-1}. K_V is the product of the trapping coefficient μ_V by the vacancy concentration C_V and $K_{V_n} = \mu_{V_n} \times C_{V_n}$ and $\mu_{V_n} = n \times \mu_V$. It follows that the total vacancy defect concentration C_V^{tot}, which is the sum of the concentration of isolated vacancies and concentration of vacancy clusters, can be estimated from equation

$$C_V^{tot} = C_V + \sum_{n=2}^{5-7} n C_{V_n} = \frac{K_{tot}}{\mu_V}. \quad (6)$$

K_{tot} could be estimated from the value of the effective diffusion length as it has been done just above for the lowest damage dose. However, the extraction of the effective diffusion length

becomes difficult for damage dose higher than 0.0085 dpa. The obtained values range between 4 and 7 nm and depends strongly to the annihilation characteristics of the second layer, in particular its thickness and the effective diffusion length. The concentration of vacancy defects cannot be determined, and it is possible to estimate a lower limit of C_V^{tot} assuming that the effective diffusion length is equal to 6 nm. In this case, C_V^{tot} would be higher or about 5×10^{26} m^{-3} for damage dose of 0.085 dpa. From 0.425 dpa, we have seen in section 3.3 that PAS results detect a saturation when the dpa level increases indicating that the types of vacancy defects detected no more change. Such saturation can be due to either the saturation of the induced damage or to the saturation of positron trapping at the detected type of defects. The values of $S_{Lay}(1)$ and $W_{Lay}(1)$ and L_{Lay} (1), and the $\left|(S_{Lay}(1)-S_L)/(W_{Lay}(1)-W_L)\right|$ ratio don't change for the highest damage doses larger or equal than 0.85 dpa indicating that if the concentration of defect would increases with damage dose the proportion of each would not evolve indicating a saturation state in the defects size distribution. Moreover, it can be observed that the thickness of the highest damage region (layer 1) increases when damage dose increases above 0.425 dpa and changes from approximately 100 nm for the lowest dpa levels to up to 170 nm for the highest ones. These results can be compared to the TDS inventory data, where overall deuterium content was found to be close for the S40 sample irradiated at 0.1 dpa (4.408×10^{19} atoms/m^2) and for the S41 sample irradiated at 0.85 dpa (3.564×10^{19} atoms/m^2). It is known that hydrogen isotopes trapping (the number of atoms in each defect type) depends on defect nature. From PAS we know that the change in the size distribution of vacancy defects is low between these two damage doses. The $\left|(S_{Lay}(1)-S_L)/(W_{Lay}(1)-W_L)\right|$ ratio is 2.10(4) for 0.085 dpa and reaches the saturation value of 2.15(4). It follows that the change in concentration of vacancy defects should be also low if we consider the H release which is even lower for the highest damage dose. It suggests that the concentration of vacancy defects reaches a saturation when irradiation induced damage becomes higher than 0.5 dpa.

A similar trend, indicating that the vacancy content in crystalline tungsten exposed to irradiation increases as a function of dose and reaches saturation at a dose above approximately 0.5 dpa, was also found in direct atomistic simulations of highly irradiated tungsten and iron performed using the creation-relaxation algorithm [53]. This simulation approach assumes a uniform spatial probability distribution of generation of defects, where at each step of execution of the algorithm, a randomly chosen atom is displaced to a random location within the simulation cell. Upon creation of a Frenkel pair, conjugate gradient minimization of the resulting atomic structure is employed to relax the position of all the atoms towards a local

potential energy minimum. The subsequent events of creation and relaxation of defect structures gradually generate microstructures whose statistical descriptors do not change with respect to further irradiation, showing no further increase of defect content as a function of dose. The dose itself, expressed in terms of the canonical dpa parameter, is defined as the ratio of the total number of Frenkel pairs created from the start of the simulation to the total number of atoms in the simulation cell. A detailed discussion of the relation between the measure of radiation exposure (dpa), related to the rate of defect production by impacts of energetic particles, and the cdpa parameter used in CRA simulations, is given in Ref. [54]. While the cdpa provides a mechanistic measure of generation of defects, applicable to a material with any structure, other measures of exposure to irradiation typically involve steps where the energy of an impact is converted into the number of defects that the impact event is expected to produce. Establishing a connection between the two parameters, cdpa and NRT dpa, involves the evaluation of the slope of a curve describing how the concentration of defects varies with the dose in the infinitely small dose limit. The corresponding procedure is illustrated in Figure 1 of Ref. [54], where an explicit link between the dpa and cdpa parameters is established.

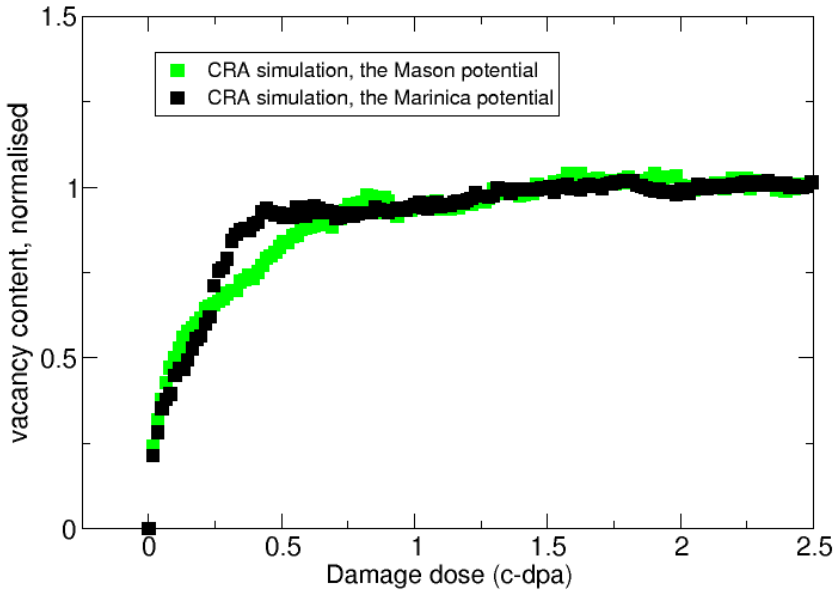

Figure 10. Variation of vacancy content in tungsten as a function of canonical dpa (c-dpa) predicted by simulations performed using the creation-relaxation algorithm (CRA) for two different interatomic potentials [53]. The values are normalised to the asymptotic high dose vacancy content, which for the Marinica potential [55] is close to 5% and for the Mason potential [56] is close to 2%.

The simulations, illustrated in Figure 10, show that after a brief period of linear accumulation that ends at ~ 0.02 dpa, the vacancy content gradually saturates as a result of build-up of internal spatially fluctuating microscopic stress caused by the defects. Similarly to the experimental curve shown in Figure 9, saturation is predicted to occur at the dose close to 0.5 dpa. Simulations also show that the density of dislocation loops in the limit of high dose is relatively low, since the majority of self-interstitial defects are now incorporated into an extended dislocation network and hence become no longer detectable by transmission electron microscopy in the form of isolated individual dislocation loops. The creation-relaxation algorithm generates microstructures that evolve solely by the relaxation of stress produced by the events of formation of Frenkel pairs, and involves no thermally activated processes. The observed saturation is the result of accumulation of high concentration of vacancies, leading to a dynamic equilibrium between the generation and annihilation of defects. Simulations show that dynamic saturation occurs at ~ 0.1 dpa [53], similar to what is found in direct cascade overlap simulations [57,58]. The validity of the pattern of microstructural evolution in tungsten derived from creation-relaxation algorithm simulations is confirmed by the observation of variation of lattice strain as a function of exposure to irradiation [59]. The origin of saturation, while related to the overlap between the spatial regions affected by collision cascades [49], is fundamentally related to the evolution of defect microstructure and occurs at a significantly higher exposure to ion irradiation than the dose of ~0.01 dpa characterising the onset of spatial overlap between the subsequent cascade events [21].

The creation-relaxation algorithm [53] simulates microstructural evolution driven by local stress and not by thermal fluctuations, and as a result it is expected that the simulations should overestimate the absolute vacancy content [59]. However, given that in irradiated tungsten vacancies do not diffuse appreciably below 350 °C [60,61], the assumption that the thermal relaxation of defect structure is impeded and effectively does not occur at room temperature, is broadly justified and agrees with direct real-space electron microscope observations of thermal annealing of extended dislocation microstructure of heavily irradiated tungsten, which remains thermally stable at temperatures up to 800 °C [62].

5. Conclusions

This study shows that tungsten irradiated to high dose at relatively low temperatures close to room temperature, and below approximately 350°C, develops a characteristic microstructure

dominated by vacancy type defects. The density of self-interstitial dislocation loops is relatively low, in agreement with recent simulations [53], suggesting that self-interstitial defects tend to incorporate themselves into an extended dislocation network that readily forms in the material at doses exceeding 0.1 dpa. At the same time, isolated vacancy defects, according to predictions derived from simulations, dominate the microstructure. The saturation of damage found in PAS agrees with simulated microstructures generated using the creation-relaxation algorithm. Implications of the observed saturation for the retention of hydrogen isotopes in irradiated tungsten and other materials are profound, and will be assessed in further work involving materials exposed to higher irradiation doses, and involving other hydrogen isotopes.

Acknowledgments

Some of the research used equipment at the UKAEA's Materials Research Facility (MRF) which is part of the UK's Henry Royce Institute and National Nuclear User Facility initiatives. We thank the MRF staff for their support. This work was supported by EUROfusion Enabling Research project TRiCEM, Tritium Retention in Controlled and Evolving Microstructure. This work has been carried out within the framework of the EUROfusion Consortium and has received funding from the Euratom research and training programme 2014-2018 and 2019-2020 under Grant Agreement No. 633053. The views and opinions expressed herein do not necessarily reflect those of the European Commission. We acknowledge funding by the RCUK Energy Programme (Grant No. EP/T012250/1).

Data availability

The raw data required to reproduce these findings are available to download from https://drive.google.com/file/d/1oLWxInUPcnJZBVeP5vdKa4B8gp0gO6_X/view. The processed data required to reproduce these findings are available to download from https://drive.google.com/file/d/1oLWxInUPcnJZBVeP5vdKa4B8gp0gO6_X/view. The raw/processed data required to reproduce the TEM and PAS results cannot be shared at this time due to time limitations and specialized software required to open the raw data. Data can be made available on request by emailing Anthony.Hollingsworth@ukaea.uk.

References

[1] M. Rieth *et al.*, Advances in Science and Technology **73**, 11 (2010).
[2] T. Hirai *et al.*, Nuclear Materials and Energy **9**, 216 (2016).

[3] M. Rieth *et al.*, Journal of Nuclear Materials **432**, 482 (2013).
[4] D.T. Blagoeva *et al.*, Journal of Nuclear Materials **442**, S198 (2013).
[5] B. Lipschultz *et al.*, Massachusetts Institute of Technology Report PSFC/RR-10-4, 2010.
[6] J. Marian *et al.*, Nuclear Fusion **57**, 092008 (2017).
[7] K. Heinola *et al.*, Phys. Rev. B **82**, 094102 (2010).
[8] K. Ohsawa *et al.*, Journal of Nuclear Materials **527**, 151825 (2019).
[9] S. Nagata and K. Takahiro, Journal of Nuclear Materials **283-287**, 1038 (2000).
[10] O.V. Ogorodnikova, Journal of Nuclear Materials **390-391**, 651 (2009).
[11] V.Kh. Alimov *et al.*, Journal of Nuclear Materials **441**, 280 (2013).
[12] T. Schwarz-Selinger, Nuclear Materials and Energy **12**, 683 (2017).
[13] B. Tyburska *et al.*, Journal of Nuclear Materials **395**, 150 (2009).
[14] B. Wielunska *et al.*, Nuclear Fusion **60**, 096002 (2020).
[15] A. Hollingsworth *et al.*, Nuclear Fusion **60**, 016024 (2020).
[16] P. Hautojärvi and C. Corbel, in: Positron Spectroscopy of Solids: Proceedings of the International School of Physics 'Enrico Fermi', A. Dupasquier and A.P. Mills Jr., (Eds.), IOS Press, Amsterdam, 1995, p. 491.
[17] A. Dupasquier and G. Ottaviani, in: Positron Spectroscopy of Solids: Proceedings of the International School of Physics 'Enrico Fermi', A. Dupasquier and A.P. Mills Jr., (Eds.), IOS Press, Amsterdam, 1995, p. 581.
[18] M.-F. Barthe, EPJ Web of Conferences **115**, 03004 (2016), https://doi.org/10.1051/epjconf/201611503004
[19] X. Yi *et al.*, Europhys. Lett. **110**, 36001 (2015).
[20] J.F. Ziegler, M.D. Ziegler, and J.P. Biersack, Nuclear Instruments and Methods in Physics Research B **268**, 1818 (2010).
[21] R.E. Stoller *et al.*, Nuclear Instruments and Methods in Physics Research B **310**, 75 (2013).
[22] http://www.SRIM.org
[23] J.-P. Crocombette and C. Van Wambeke, EPJ Nuclear Sciences and Technologies **5**, 7 (2019).
[24] D.R. Mason *et al.*, Journal of Physics : Condensed Matter **26**, 375701 (2014).
[25] O.V. Ogorodnikova *et al.*, Physics Procedia **71**, 41 (2015), https://doi.org/10.1016/j.phpro.2015.08.309
[26] M.T. Robinson and I.M. Torrens, Physical Review B **9**, 5008 (1974).
[27] D.R. Mason *et al.*, Acta Materialia **144**, 905 (2018).
[28] K. Arakawa *et al.*, Nature Materials **19**, 508 (2020), https://doi.org/10.1038/s41563-019-0584-0
[29] J. Wang *et al.*, Journal of Nuclear Materials **545**, 152749 (2021).
[30] M. Zibrov *et al.*, Journal of Nuclear Materials **477**, 292 (2016).
[31] O.V. Ogorodnikova, Journal of Applied Physics **118**, 074902 (2015).
[32] S. Markelj *et al.*, Nuclear Fusion **59**, 086050 (2019).
[33] W.M. Shu, E. Wakai, and T. Yamanishi, Nuclear Fusion **47**, 201 (2007).
[34] Y. Zayachuk *et al.*, Nuclear Fusion **53**, 013013 (2013).
[35] P. Desgardin *et al.*, Materials Science Forum **363-365**, 523 (2001).
[36] A. van Veen *et al.*, AIP Conference Proceedings **218**, 171 (1990).
[37] A. Vehanen *et al.*, Physical Review B **29**, 2371 (1984).

[38] P.J. Schultz and K.G. Lynn, Reviews of Modern Physics **60**, 701 (1988).
[39] T. Troev *et al*., Nuclear Instruments and Methods in Physics Research B **267**, 535 (2009).
[40] Y. Xu *et al*., Modern Physics Letters B **17**, 147 (2003).
[41] P.E. Lhuillier *et al*., Physica Status Solidi C **6**, 2329 (2009).
[42] A. Debelle, M.-F. Barthe, and T. Sauvage, Journal of Nuclear Materials **376**, 216 (2008).
[43] P. Staikov and N. Djourelov, Physica B: Condensed Matter **413**, 59 (2013).
[44] Y.-K. Park *et al*., Phys. Rev. B **34**, 823 (1986).
[45] T.E.M. Staab *et al*., Journal of Physics : Condensed Matter **11**, 1787 (1999).
[46] E. Kuramoto *et al*., Computational Materials Science **14**, 28 (1999).
[47] W. Asplet, "Experimental study of the interaction of vacancy defects with Y, O and Ti solutes to better understand their roles in the nanoparticles formation in ODS steels", PhD thesis supervised by M.-F. Barthe, Orléans, Université d'Orléans, 2018, https://tel.archives-ouvertes.fr/tel-02395001
[48] M. Sidibe, "Study of the behaviour of tungsten under irradiation: application to fusion reactors", PhD thesis supervised by M.-F. Barthe, Orléans, Université d'Orléans, 2014, https://tel.archives-ouvertes.fr/tel-01068634
[49] O.V. Ogorodnikova and V. Gann, Journal of Nuclear Materials **460**, 60 (2015).
[50] O.V. Ogorodnikova *et al*., Nuclear Fusion **57**, 036011 (2017).
[51] R. Krause-Rehberg *et al*., Nuclear Instruments and Methods in Physics Research B **240**, 719 (2005).
[52] X. Yi *et al*., Acta Materialia **112**, 105 (2016).
[53] P.M. Derlet and S.L. Dudarev, Physical Review Materials **4**, 023605 (2020).
[54] D. R. Mason *et al*., Physical Review Materials **5**, 095403 (2021).
[55] M.-C. Marinica *et al*., Journal of Physics: Condensed Matter **25**, 395502 (2013).
[56] D.R. Mason, D. Nguyen-Manh, and C.S. Becquart, Journal of Physics : Condensed Matter **29**, 505501 (2017).
[57] F. Granberg *et al*., Physical Review Letters **116**, 135504 (2016).
[58] L. Koch *et al*., Journal of Applied Physics **122**, 105106 (2017).
[59] D. Mason *et al*., Physical Review Letters **125**, 225503 (2020).
[60] M.W. Thompson, Philosophical Magazine **5**, 278 (1960).
[61] J. Heikinheimo *et al*., APL Materials **7**, 021103 (2019)
[62] F. Ferroni *et al*., Acta Materialia **90**, 380 (2015).

Comparative study of deuterium retention and vacancy content of self-ion irradiated tungsten

A. Hollingsworth[a*], M.-F. Barthe[b], M.Yu. Lavrentiev[a], P.M. Derlet[c], S.L. Dudarev[a], D.R. Mason[a], Z. Hu[b], P. Desgardin[b], J. Hess[a], S. Davies[a], B. Thomas[a], H. Salter[a], E.F.J. Shelton[a], K. Heinola[de], K. Mizohata[d], A. De Backer[a], A. Baron-Wiechec[a,f,g], I. Jepu[h], Y. Zayachuk[a], A. Widdowson[a], E. Meslin[i], A. Morellec[i]

[a]*UK Atomic Energy Authority, CCFE, Culham Science Centre, Abingdon, Oxon, OX14 3DB, United Kingdom*
[b]*CNRS, CEMHTI UPR3079, Univ. Orléans, F-45071 Orléans, France*
[c]*Condensed Matter Theory Group, Paul Scherrer Institut, CH-5232, Villigen PSI, Switzerland*
[d]*Department of Physics, University of Helsinki, 00560 Helsinki, Finland*
[e]*International Atomic Energy Agency, A-1400, Vienna, Austria*
[f]*Technion – Israel Institute of Technology, Haifa 32000, Israel*
[g]*Guangdong Technion – Israel Institute of Technology, Shantou 515063, PR China*
[h]*Laboratory of Low Temperature Plasma, National Institute for Laser, Plasma and Radiation Physics, Magurele, Romania*
[i]*DEN-Service de Recherches de Métallurgie Physique, CEA, Université Paris-Saclay, F-91191, Gif-sur-Yvette, France*

Abstract

Self-ion irradiation of pure tungsten with 2 MeV W ions provides a way of simulating microstructures generated by neutron irradiation in tungsten components of a fusion reactor. Transmission electron microscopy (TEM) has been used to characterize defects formed in tungsten samples by ion irradiation. It was found that tungsten irradiated to 0.85 dpa at relatively low temperatures develops a characteristic microstructure dominated by dislocation loops and black dots. The density and size distribution of these defects were estimated. Some of the samples exposed to self-ion irradiation were then implanted with deuterium. Thermal Desorption Spectrometry (TDS) analysis was performed to estimate the deuterium inventory as a function of irradiation damage and deuterium release as a function of temperature. Increase of inventory with increasing irradiation dose followed by slight decrease above 0.1 dpa was found. Application of Positron Annihilation Spectroscopy (PAS) to self-irradiated but not deuterium implanted samples enabled an assessment of the density of irradiation defects as a function of exposure to high-energy ions. The PAS results show that the density of defects saturates at doses in the interval from 0.085 to 0.425 displacements per atom (dpa). These

*Corresponding author. Email: Anthony.Hollingsworth@ukaea.uk

results are discussed in the context of recent theoretical simulations exhibiting the saturation of defect microstructure in the high irradiation exposure limit. The saturation of damage found in PAS agrees with the simulation data described in the paper.

1. Introduction

Tungsten has relatively high thermal conductivity, high sputtering resistance, and mechanical strength at high temperatures. These properties have favoured its selection as the primary candidate material for the divertor of ITER [1,2], as well as a prospective material for the divertor and first wall components in DEMO [3,4]. It is expected that in ITER and DEMO tungsten will be exposed to extreme operating conditions, including direct contact with fusion plasma as well as high neutron flux. The challenges associated with the operation of tungsten components include making a quantitative characterization of the effects of the operating environment and understanding the evolution of mechanical properties as well as providing a realistic estimate of tritium retention. Retention of hydrogen and its isotopes is known to alter the physical and mechanical properties of materials, and the loss of radioactive tritium inventory is problematic both in terms of fuel efficiency and regulatory constraints [5]. Furthermore, exposure to high energy ions and neutrons gives rise to displacement cascades and production of defects in the microstructure. This requires investigating the damage that irradiation generates in tungsten, including the production of defects (vacancies and interstitials), their complexes (cavities and loops), and extended dislocation network. One of the significant questions related to the assessment of hydrogen isotope retention is the evaluation of how the density of defects, particularly vacancies, depends on the irradiation dose, since vacancies and vacancy clusters are known to act as traps for hydrogen isotopes and helium [6-8].

Deuterium retention in tungsten has been subject of numerous studies. Often, a single method of characterization has been used, such as elastic recoil detection [9], TDS [10], or nuclear reaction analysis (NRA) [11,12]. Combination of TDS and scanning electron microscopy morphology study was performed by Tyburska *et al*. [13]. Wielunska *et al*. [14] performed a combined TDS and NRA study of retention in tungsten irradiated by different ions. In this paper, we describe an experimental study of self-irradiated tungsten that uses several techniques and is supported by theoretical analysis and simulations. The study was performed within the UKAEA-led Europe-wide Tritium Retention in Controlled and Evolving Microstructure (TRiCEM) project. Some of the tungsten samples were exposed to deuterium plasma at room temperature in a new facility that enables studying the interaction of hydrogen isotopes with nuclear fusion relevant first wall materials, as well as the retention and release of

these isotopes. The new facility enables the implantation of a range of gases into the samples, including tritium. The design of this facility and the commissioning results are described in detail in a recent publication [15]. After implantation, the samples were studied using several experimental techniques, including Thermal Desorption Spectroscopy (TDS) and Transmission Electron Microscopy (TEM). Our aim is to identify peaks in the TDS spectra of irradiated tungsten, to investigate the dependence of deuterium inventory on irradiation damage, and to compare the data with earlier experimental results. Next, we performed Positron Annihilation Spectroscopy (PAS) analysis of the samples, as PAS is an established technique for the detection of vacancy-type defects [16-18]. PAS is sensitive to small defects from a single vacancy to vacancy clusters and has lower detection limit (depending on the material and the nature of the defects) in the range from about 10^{23} m^{-3} down to about 10^{20} m^{-3}, hence enabling a fairly precise determination of the density of defects.

The paper is organized as follows. In Section 2, we describe the preparation of samples used in this study, and their characterization using electron microscopy and TDS. In Section 3, we present the results of PAS analysis and give estimates for the level of damage as a function of irradiation dose. We discuss the results and their relation to recent developments in modelling and simulation of defects in materials in Section 4 and conclude in Section 5.

2. Material preparation and characterization

2.1. Preparation

Hot-rolled, 99.95% purity guaranteed pure sheet sections of tungsten were purchased from Plansee. The material was annealed in a vacuum (6×10^{-6} mbar) furnace for 20 hours at 1500°C. Circular discs of 500 µm thickness were cut using a Struers cutting saw. The samples were then polished in several stages with abrasive SiC paper form FEPA P250 to P4000 to 100 µm thickness, producing a flat surface with a thin deformation layer. Chemo-mechanical polishing using colloidal silica suspension (0.05 microns) has been used to obtain a mirror surface finish. The polished samples were then cleaned in an ultrasonic bath with iso-propanol for 15 minutes and then acetone for a further 15 minutes. Discs of 3 mm diameter were punched out from the polished specimen. Then, two types of specimen were electropolished. Specimens prepared for TEM characterisation before irradiation were double-side jet electropolished in a Tenupol-5 thinning device to produce electron-transparent thin foils. The polishing bath was composed of 2 g NaOH in 1 litre of demineralized water following Yi *et al*. [19]. Specimens prepared for

irradiation were only one-side jet electropolished for a few seconds to obtain mirror finished dimpled discs. After irradiation, the irradiated side has been protected with a varnish and TEM thin foil has been obtained by back-electropolishing using the same electrolyte as used before irradiation. The thickness of the analysed area was around 100 nm, as determined by classical thickness fringes method. Dimpled discs prepared for irradiation were shipped to the accelerator laboratory at the University of Helsinki where damage was produced by the exposure to high energy ions. Irradiation was performed using raster-scanned beam at room temperature. The ion species used for this work are 2 MeV W^+. The dependence of damage (measured in displacements per atom, dpa) as a function of depth from the surface is shown in Figure 1. It was calculated for the total fluence of 1×10^{18} ion/m^2, using two methods: the SRIM software [20-22] and the Iradina [23] codes using the Kinchin-Pease model as suggested in [21] assuming the displacement threshold energy E_d = 55 eV [24,25]. The maximum damage at around 75 nm from the surface was found to be close to 0.85 dpa. With another commonly used value of the threshold energy E_d = 90 eV, this dpa value, as well as all other damage levels given in this paper would have been reduced by about 1.6 times.

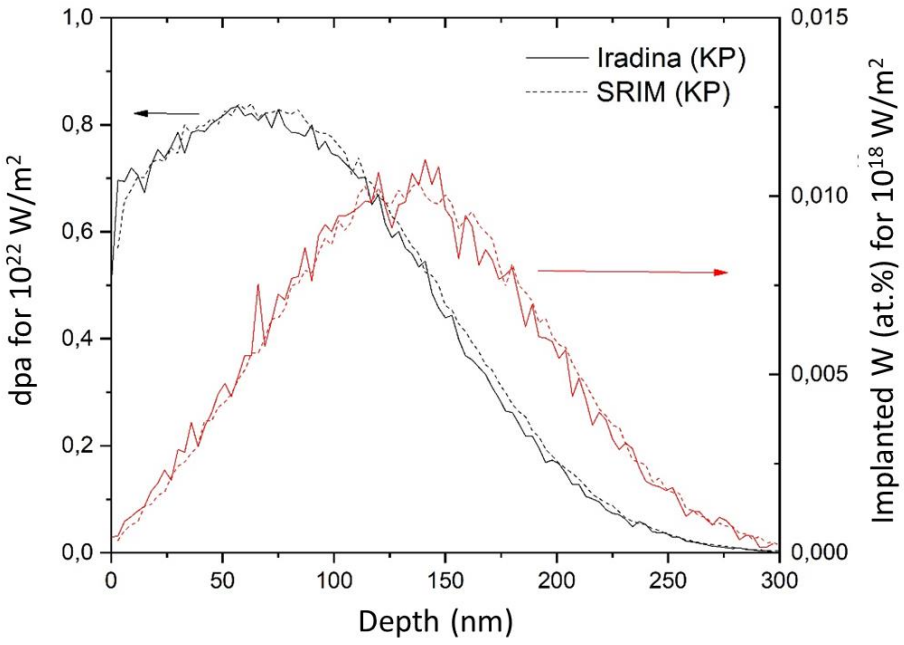

Figure 1. Damage profile (in dpa, left axis), and the density of implanted ions per unit area in the samples irradiated up to the total fluence of 1×10^{18} ion/m^2. The calculations use the Kinchin-Pease formula and were performed using the SRIM [20-22] and Iradina [23] codes, both based on the binary collision approximation [26].

The samples used in this study are described in Table 1. Deuterium implanted samples were used for TDS and TEM studies, whereas un-implanted samples were studied using Positron Annihilation Spectroscopy method.

Sample	Irradiation fluence (2 MeV W^+), atoms/m^2	Irradiation time (s)	Self-irradiation dose (dpa)	Deuterium implanted?	Characterization
S17	0	0	0	Yes	TDS
S37	0	0	0	Yes	TDS
S40	1×10^{18}	180	0.85	No	TEM
				Yes	TDS
S41	1.2×10^{17}	19	0.102	Yes	TDS
S42	1.8×10^{16}	3	0.0153	Yes	TDS
S112	0	0	0	No	PAS
S113	1×10^{16}	53	0.0085	No	PAS
S116	1×10^{17}	477	0.085	No	PAS
S119	5×10^{17}	2289	0.425	No	PAS
S123	1×10^{18}	4424	0.85	No	PAS
S125	2×10^{18}	8406	1.7	No	PAS

Table 1. List of the samples used in the current study.

2.2. Electron Microscopy

A conventional FEI 20 G2 Tecnai Transmission Electron Microscope, located at CEA Saclay and equipped with a LaB_6 source delivering 200 keV electrons, was used. Bright Field (BF) and Weak Beam Dark Field (WBDF) images were recorded to study irradiation features such as dislocation loops and lines. A camera Gatan Orius 200D has been used to record images and movies. The latter were recorded at a rate of 30 images per second.

Before irradiation, the material presented a typical annealed structure, composed of micrometric grains with low density of dislocation lines (~$10^{12}/m^2$) (Figure 2). The mean grain size, as determined by scanning electron microscopy (SEM), was about 90 µm, although much smaller grains were also present (Figure 2, right).

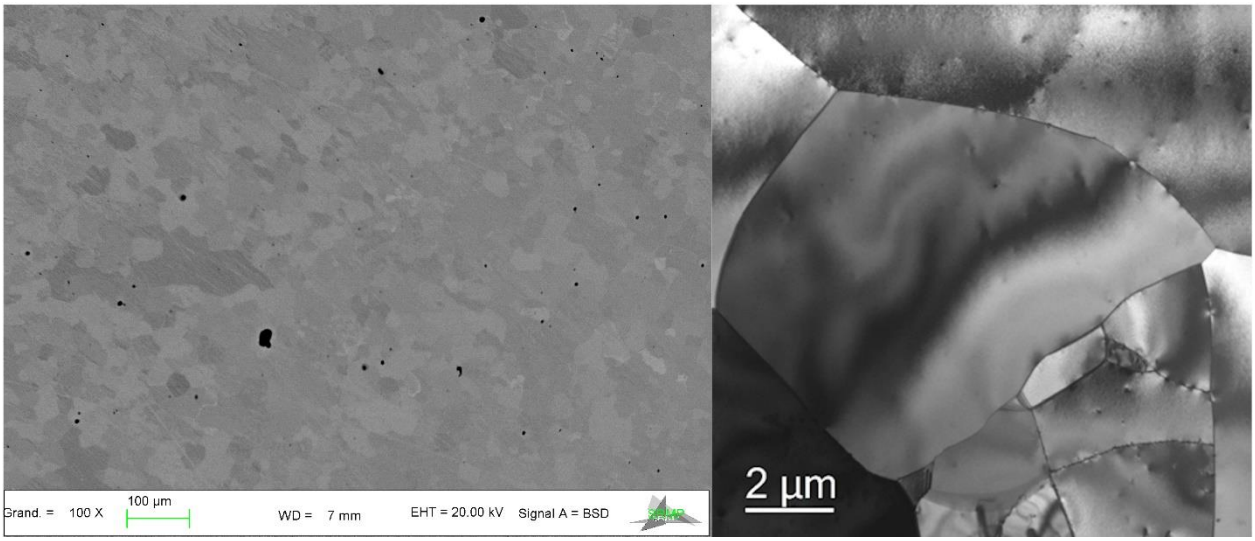

Figure 2. TEM images of electropolished tungsten before irradiation (BF image).

After irradiation, the formation of high density of irradiation defects was detected (Figure 3). They are in the form of dislocation loops and black dots. An automated analysis of the visible features seen in this region has been performed to determine the size distribution of defects. The same method as in the procedure outlined in Appendix A of [27] has been used, as shown in the Figure 4. Altogether, 1279 objects have been considered for the measurements. The mean size and volume density of defects are equal to 3.4±0.1 nm and $(3.94\pm0.1)\times10^{13}$ loops/m², respectively. A statistical error is also shown.

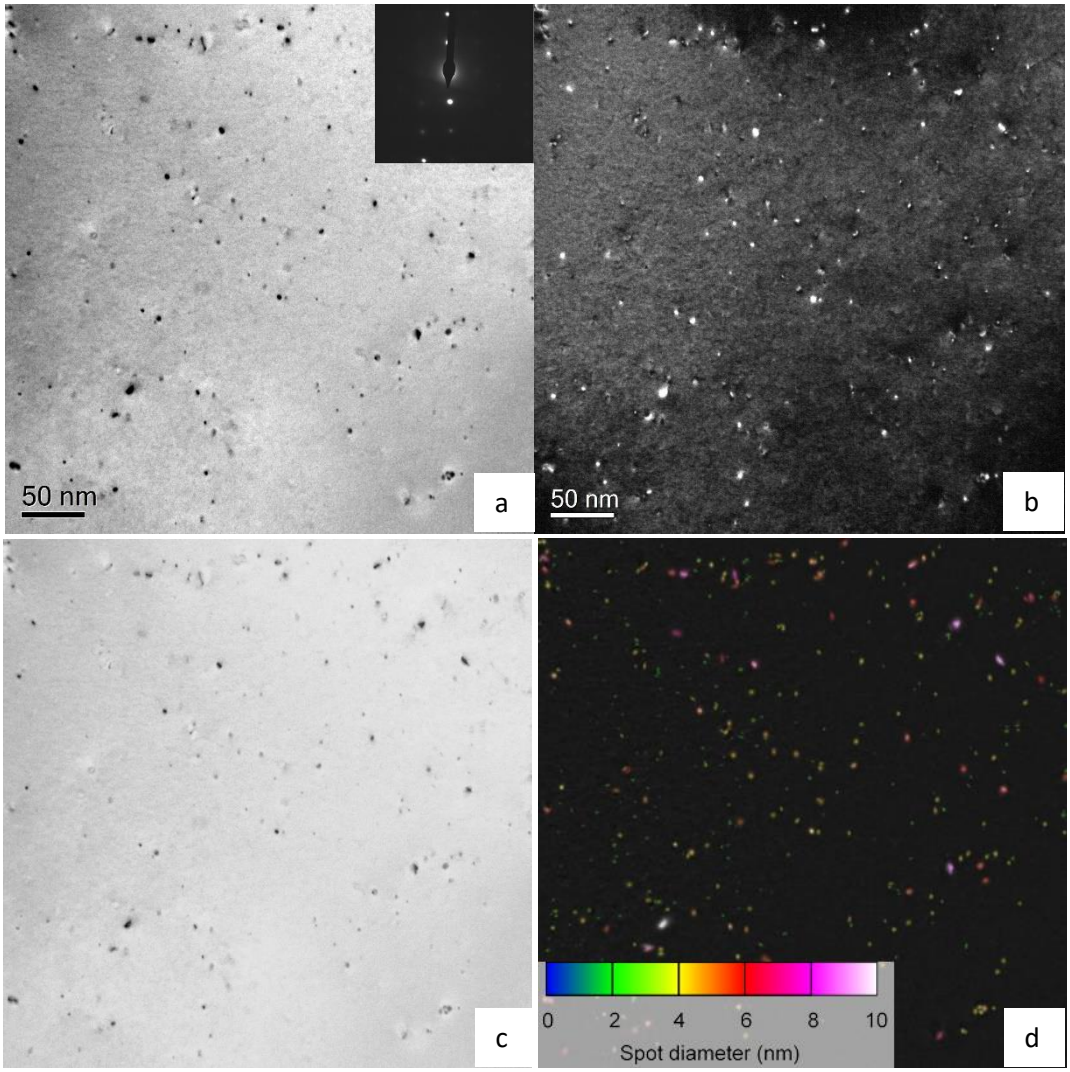

Figure 3. BF (a) and WBDF images (b) of tungsten irradiated up to 0.85 dpa at peak at room temperature. Images were performed in a <001> zone axis by using a <011> type diffracting vector. (c) and (d): the same images with the background subtracted and identified defects obtained by D. Mason's code [27].

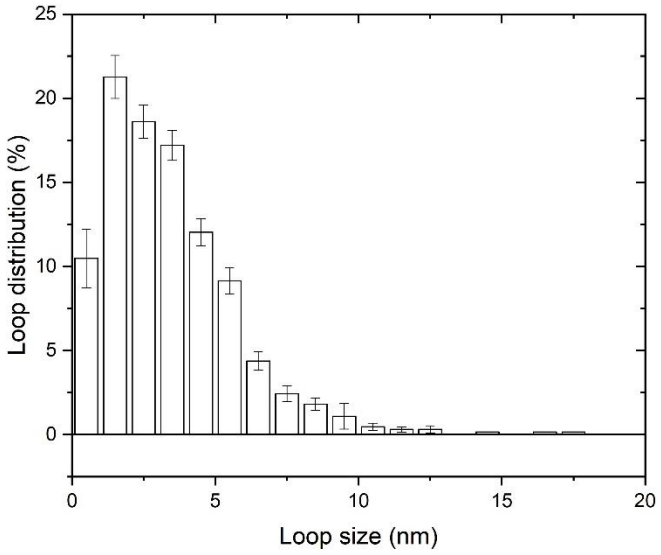

Figure 4. Size distribution of the loops formed in tungsten irradiated up to 0.85 dpa at peak at room temperature. BF images has been used to obtain the distribution.

An electron beam induced defect mobility has also been noted during the observation with 200 keV electrons at room temperature. Examples of loop jumps are given in Figure 5. Similar mobility was reported recently [28].

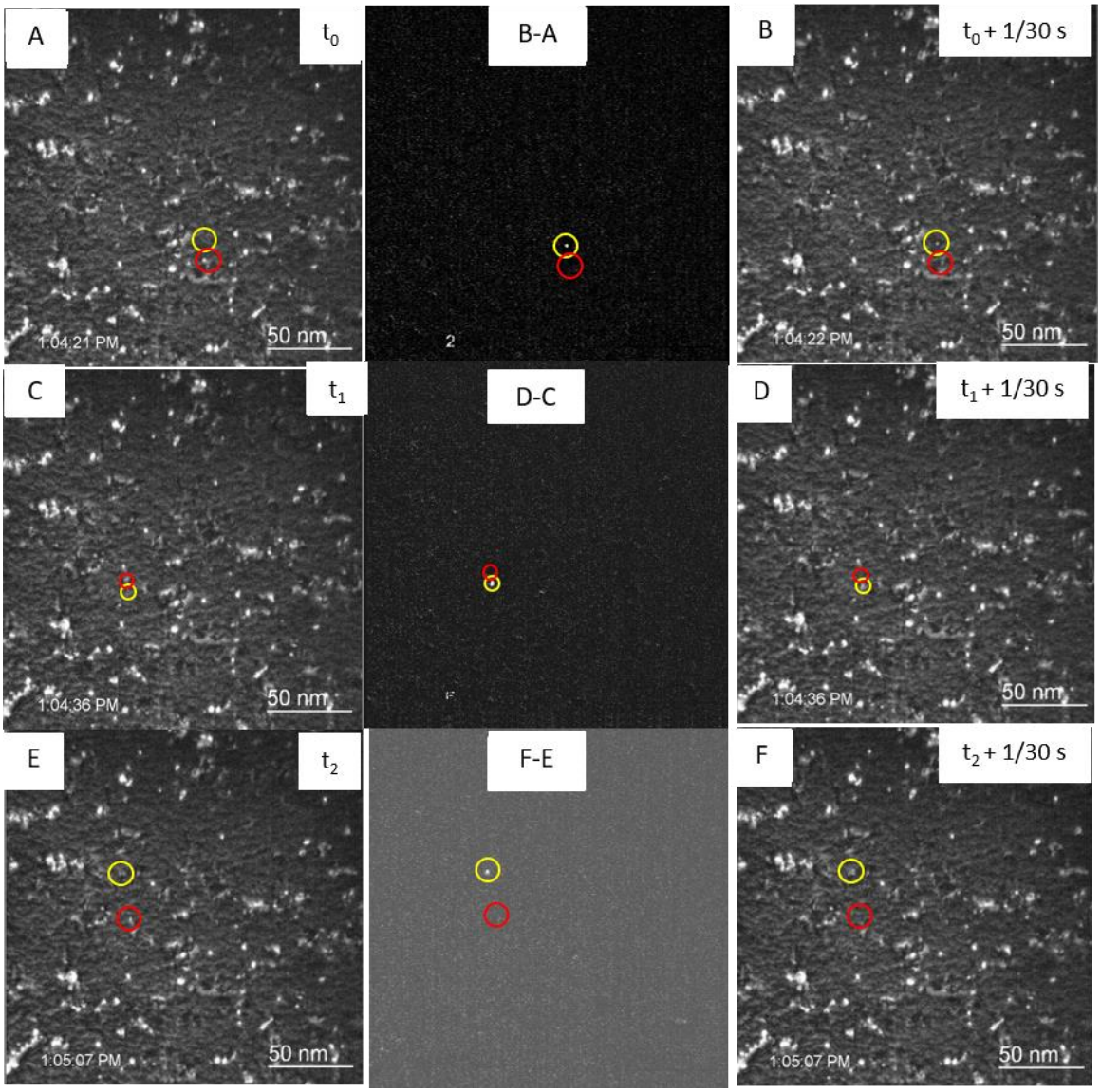

Figure 5. Three series of images extracted from the observation using 200 keV electron beam in tungsten irradiated up to 0.85 dpa at peak at room temperature (WBDF image, **z**=<001>, **g**=<110>). An example of image subtraction is shown in the middle to highlight the loop jump between A and B, C and D, and E and F frames. The initial position of the moving loop is highlighted by red circles in all the images, whereas the final position of the loop is highlighted by yellow circles.

2.3. Thermal Desorption Spectrometry

After exposure to deuterium plasma up to an estimated fluence of 10^{23} D/m^2, with ion energy 400 eV and sample's surface temperature 50 °C, TDS measurements were performed on the implanted samples using Hiden Analytical Type 640100 TPD workstation. Linear temperature ramp from room temperature to 1000°C was used, with a constant heating rate of 10 K/min. Release signals of deuterium-containing molecules – HD (mass 3) and D_2 (mass 4) were recorded using line-of-sight quadruple mass spectrometer; these were quantified using calibrated hydrogen and deuterium leaks, with calibration factor for HD signal being the average between the factors for H_2 and D_2. Total atomic deuterium release was then calculated as a sum of molecular release signals, namely $F_{atomic}(D)=F_{molecular}(HD)+2*F_{molecular}(D_2)$. The overall inventory is given in Table 2. The total deuterium retention for unirradiated samples rapidly decreases with time after the exposure, falling by almost a half after 14 days (samples S17, S37). For the irradiated samples, the total retention rises with irradiation dose up to 0.102 dpa (S41), then falls by around 20% in sample S40 irradiated to 0.85 dpa. We estimate the error of TDS inventory measurements to be ±10%, based on analysis of several identical reference samples. This alone, or combined with a difference in delay time, is not sufficient to explain the difference between the 0.102 dpa and 0.85 dpa total retention. One possible explanation for further decrease is a slight offset of the spectrum of the 0.85 dpa sample on the temperature axis compared to the other samples (Figure 6). Offsets on this axis are likely due to differences in mounting on the heating stage of the TDS. This may have led to an underestimate of the deuterium retention in the 0.85 dpa sample. On the other hand, it might be a genuine effect, deserving further study. Similar decrease of retention was found in a recent nuclear reaction analysis study of W samples irradiated to 0.5 and 5 dpa ([29], Figure 2). In any case, it is clear from the TDS results that there is no significant increase in retention between the 0.102 dpa and 0.85 dpa samples, despite an order of magnitude difference in irradiation dose. This is broadly in line with the saturation of vacancy density observed in the PAS results discussed below.

The resulting TDS spectra are shown in Figure 6. Several characteristic temperature regions can be identified, in which there are notable differences between the unirradiated and irradiated samples. The first region is a wide maximum between 350-400 K and 550-600 K, present in the spectra of all the samples. In the irradiated samples (S40-S42) the higher temperature peak

contains more deuterium, whereas in the un-irradiated samples (S17 and S37) the ratio is significantly different. The substantial decrease of the low-temperature peak in un-irradiated

Sample	Self-irradiation dose (dpa)	Delay time between deuterium exposure and TDS (days)	Total deuterium inventory ($x10^{19}$ atoms/m^2)
S17	0	1	4.693
S37	0	14	2.594
S42	0.0153	43	2.589
S41	0.102	47	4.408
S40	0.85	49	3.564

Table 2. Total deuterium inventory of the samples analysed by TDS.

sample S37 compared to S17 can be attributed to a longer delay between implantation and TDS measurements for S37, allowing the weakly bound deuterium to be released. It should be noted that the spectra of irradiated samples feature this low-temperature release stage even though the delay between D implantation and TDS measurement was significantly longer. This allows making a distinction between several kinds of traps with similar trapping energies – some of which are caused by irradiation while others are intrinsic and are present even in the unirradiated material. This maximum has been detected previously in the case of low-temperature implantation [30] and it was suggested that it might be attributed to release of deuterium from several possible weak traps, such as grain boundaries or surface adsorption sites; these are the abovementioned intrinsic defects. On the other hand, vacancies with multiple occupancy might contribute to desorption in this temperature range for irradiated samples, as it was shown that as the occupancy of traps increases, the binding energy of hydrogen isotopes decreases [7,8]. These are possible candidates for the irradiation-induced traps.

A second region is characterized by a narrow peak centered around 700-750 K, in agreement with results reported elsewhere [30-32]. This peak is present in all release spectra; however, it is evident that its magnitude significantly increases for the pre-damaged samples as compared with unirradiated ones, which indicates that this peak is associated with the defects introduced by displacement damage due to high-energy ion irradiation. The height of this peak increases with the increase of irradiation dose to 0.1 dpa. Usually, this peak is attributed to deuterium release from single vacancies. It is important to stress here the role of delay between

implantation and the TDS. In particular, the comparison of TDS spectra between two unirradiated samples: S17 (next day TDS), and S37 (TDS 14 days after exposure) shows large decrease of the 750 K peak. Even the smallest irradiation dose of 0.0153 dpa (sample S42) results in higher 750 K peak than in S37, despite even longer delay between exposure and the TDS (43 days). This confirms creation of single vacancies at very low irradiation doses.

Finally, a small broad peak was detected at around 1100 K in all the irradiated samples, with its height increasing with the increase of irradiation dose, while at the same time it is absent in the non-irradiated ones. Again, this indicates that this peak is associated with deuterium trapping on the defects associated with the displacement damage. In the literature release peak at this temperature is attributed to the release of deuterium from the gas-filled under-surface voids or vacancy clusters [33,34].

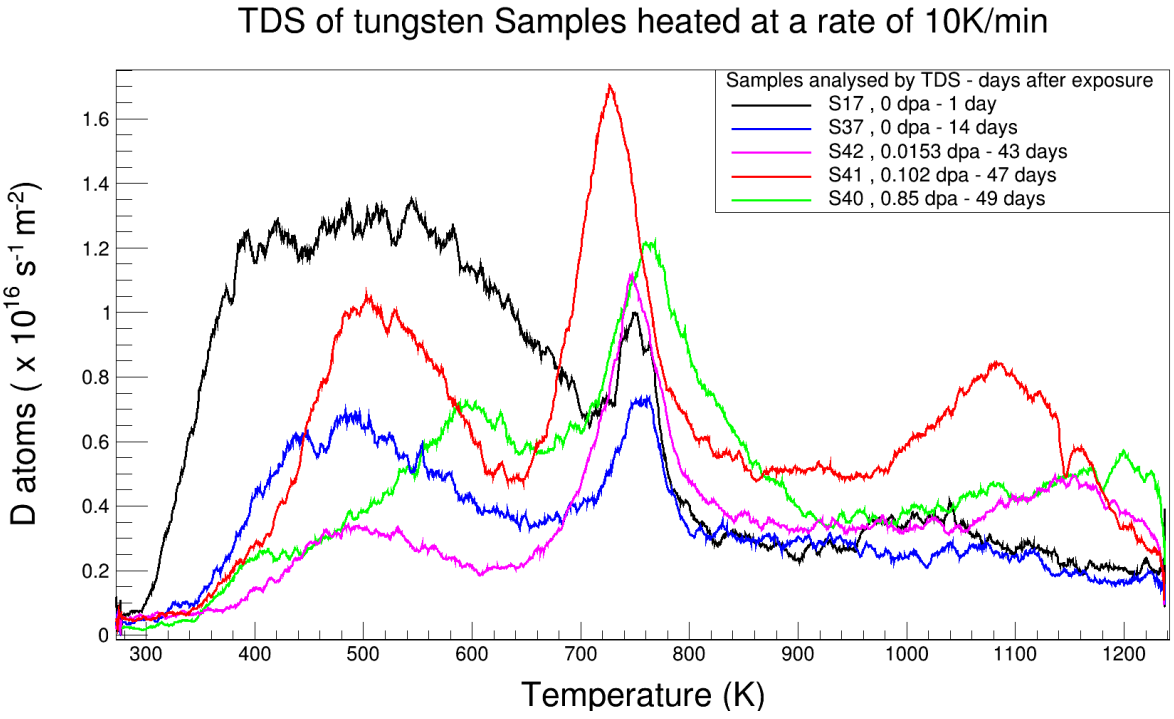

Figure 6. TDS spectra of implanted samples with damage levels between 0 and 0.85 dpa. Time period between exposure to deuterium plasma and the TDS is shown in the inset.

3. PAS Analysis

3.1. Description of the PAS system and method used

The samples were characterized by using a slow positron beam coupled to a Doppler broadening spectrometer (SPB-DB) available at the CEMHTI laboratory. A comprehensive description of the experimental setup and the basics of this powerful method are described in [35]. A monoenergetic positron beam, with a diameter of 3 mm, was generated from a ^{22}Na source. The energy of the beam was varied in the range of 0.5 to 25 keV. The spectrum of the γ-ray annihilation photons (centered at 511 keV) coming from the sample is recorded using a high-resolution gamma spectrometer equipped with a germanium detector (1.24 keV resolution at 514 keV). This Doppler broadened spectrum is characterized by two line-shape parameters: *S* and *W*. *S*, defined as the ratio of counts in the central region of the spectrum to the total counts, represents the fraction of positron-electron pairs annihilated with low momentum and is thus related mostly to annihilations with valence electrons. *W*, the ratio of counts in the wing regions of the spectrum to the total counts, represents the fraction of positron-electron pairs annihilated with high momentum and hence is more specifically related to the annihilations of positrons with core electrons. For our experiments, the momentum ranges for the calculation of *S* and *W* are 0-$\left|2.80\right|\times10^{-3}\ m_e c$ and $\left|10.61\right|\times10^{-3}$ - $\left|26.35\right|\times10^{-3}\ m_e c$, respectively, where m_e is the electron mass and *c* the speed of light. These momentum ranges correspond to ranges of energies of photons emitted as a result of annihilation of 510.28 – 511.72 keV for the *S* photons, and 504.27 – 508.29 keV and 513.71 – 517.73 keV for the *W* photons. Each material exhibits specific S_L and W_L values, as a signature of the momentum distribution of electrons in the perfect lattice in the absence of vacancy defects. The sensitivity of the PAS technique to the type and concentration of vacancy defects in solids is based on the fact that positrons are more susceptible to being trapped at open volume defects where the electron density is low, before annihilation [16]. When positrons are trapped at vacancies, their smaller overlap with core electrons narrows the positron-electron momentum distribution, resulting in an increase of *S* and decrease of *W*. Hence *S* and *W* yield information about the presence of vacancy defects in solids as parameter *S* increases and *W* decreases. Each type of vacancy cluster *j* is characterized by some specific values of S_j and W_j. Generally, *S* increases and *W* decreases when the number of vacancies *n* in the cluster V_n increases.

For this study, *S(E)* and *W(E)* were recorded as functions of positron energy *E* spanning the range from 0.5 to 25 keV. This energy range corresponds to the mean positron implantation

depth in tungsten between approximately 0.4 and 300 nm. Note that the full-width-at-half-maximum of the implanted positrons distribution increases with the energy, to reach ≈ 380 nm at 25 keV. At this energy, positrons probe up to ≈ 700 nm depth below the tungsten surface, i.e. all the damaged region, as can be seen in Figure 7. The *S* value measured at energy *E* depends on the defect distribution and diffusion properties of the positrons in the sample. A modified version of VEPFIT program [36] allows the calculation of *S(E)* and *W(E)* taking into account positrons implantation and their diffusion, assuming that the defect depth profile is a sequence of homogeneous layers. Note that the diffusion of positrons is limited by their trapping at defects and hence the effective diffusion length that L_{eff}^{+} can be written as follows [37]:

$$L_{eff}^{+} = \sqrt{\frac{D^{+}}{\lambda_L + \sum_{j=1}^{m} K_j}} \quad (1)$$

where K_j are the positron trapping rates at various detected defects (single vacancy, vacancy clusters V_n, dislocations etc.), D^+ is the intrinsic positron diffusion coefficient ($D^+ = 1.26\times10^{-4}$ m^2/s for tungsten [38]), and λ_L the lattice annihilation rate ($\lambda_L = 1/\tau_L$, τ_L= 101-105 ps [39,40]). Hereafter, VEPFIT is used for consistently fitting the *S(E)* and *W(E)* curves allowing the extraction of the *S(z)* and *W(z)* depth profiles and the effective diffusion length in each layer. Note that the data for the positron energy below 2.0 keV were discarded because for this low energy, the positron's migration does not result, in the present case, in a diffusion process.

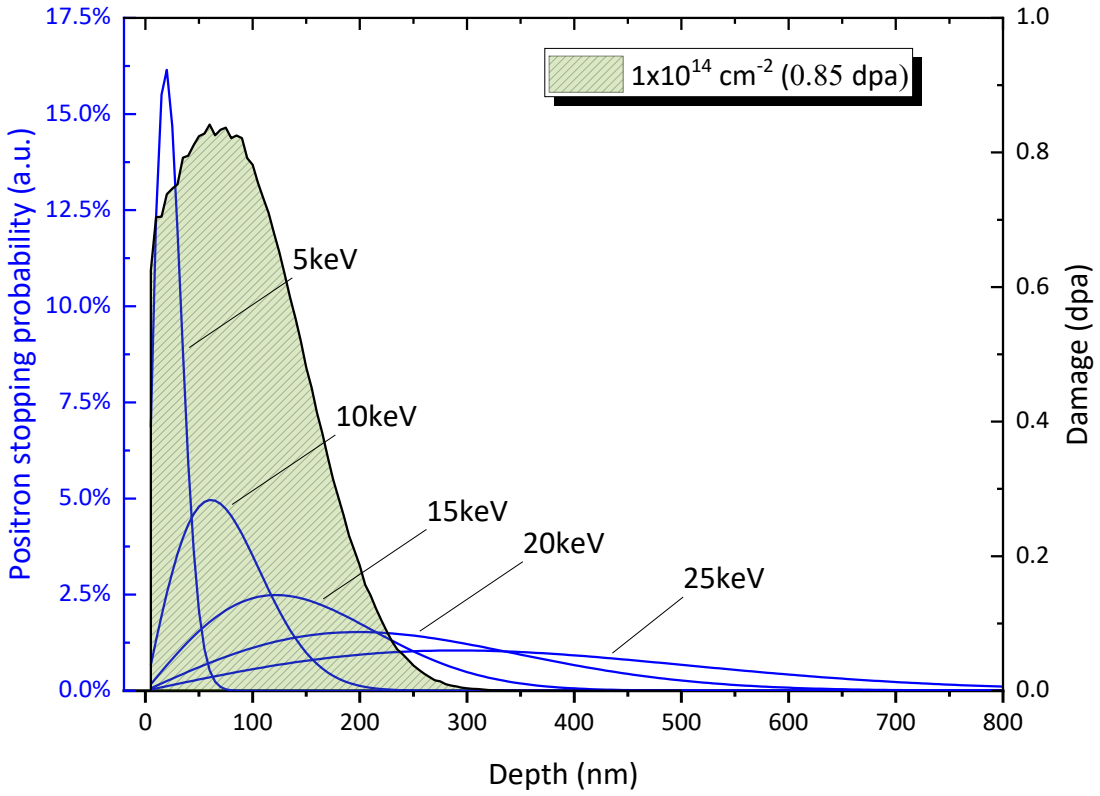

Figure 7. Implantation profiles of 5, 10, 15, 20 and 25 keV positrons in tungsten compared to the SRIM calculations of the damage profile of 2 MeV W^+ ions implanted at a 1×10^{14} atoms/cm^2 fluence at room temperature, taking a displacement threshold energy of 55 eV [24,25] in the Kinchin-Pease model as recommended by Stoller *et al.* [21].

The line-shape parameter $S(z)$ (or in the case where the vacancy defect depth profile is modelled as a succession of homogeneous layers, $S_{lay}(i)$ corresponding to the S value in layer i) is related to the specific values S_j of the trapping defects j at which positrons are annihilating and the fraction of annihilation of these defects f_j as given in equation (2) below. Also, $W(z)$ (or $W_{lay}(i)$) can be expressed in the same way:

$$S_{lay}(i) = f_L \times S_L + \sum_{j=1}^{m} S_j \times f_j, \qquad W_{lay}(i) = f_L \times W_L + \sum_{j=1}^{m} W_j \times f_j, \qquad (2)$$

where the specific annihilation fractions f_L for annihilation in the lattice and f_j for the case of positron trapping at traps j from which no detrapping can occur because the trapping energy at these traps is high enough for the measurement temperature [10], can be written as follows:

$$f_L = \frac{\lambda_L}{(\lambda_L + \sum_{j=1}^{m} K_j)}, \qquad f_j = \frac{K_j}{(\lambda_L + \sum_{j=1}^{m} K_j)} \qquad (3)$$

$S_{lay}(i)$ and $W_{lay}(i)$ values are related to the total positron trapping rate K_j at the detected defects j. K_j is the product of the traps concentration C_j by their specific trapping coefficient μ_j. The

specific trapping coefficient μ_V of single vacancy in tungsten is approximated to the value determined for the single vacancy in Ta which has Z value close to tungsten ($\mu_V = 6 \pm 3 \times 10^{-9}$ cm^3/s [16]). It is expected that the specific trapping coefficient for vacancy clusters V_n is n times the trapping coefficient of a single vacancy ($\mu_{Vn} = n \times \mu_V$) when n is lower than 10 [16].

Some annihilation characteristics have been already experimentally determined in tungsten. For the perfect lattice, the annihilation characteristics are $S_L = 0.367(4)$ and $W_L = 0.084(5)$; for the single vacancy, $S_V = 0.417(1)$ and $W_V = 0.057(1)$ [41,42]. The $\left| (S_V - S_L)/(W_V - W_L) \right|$ ratio is equal to 1.85(3) and can be assigned to annihilation of positrons as trapped at single vacancy. The annihilation characteristics S_{Vn}, W_{Vn} of vacancy clusters are not known, only for some V_n positron lifetimes (τ_{Vn}) have been already calculated [39]. τ_{Vn} increases with n, meaning that it increases as a function of the size of a vacancy cluster. τ_{Vn} becomes constant when n is so high that the positron annihilates close to the surface of the cluster, as the electron density is negligible inside the vacancy cluster. Saturation occurs when n becomes larger than 20 vacancies [39]. The maximum and minimum values of line-shape parameters were obtained in earlier studies that we carried out in tungsten and are as follows: $S_{Max} = 0.5026$, $W_{Min} = 0.0364$. S_{Max} and W_{Min} are most probably related to the annihilation in vacancy clusters with the maximum size detectable with SPB-DB that means V_N where N is equal or larger than 20 as it has been also observed for the positron lifetime in the theoretical study from [39]. The $\left| (S_{max} - S_L)/(W_{min} - W_L) \right|$ ratio (equal to 2.8) can be assigned to annihilation in vacancy cluster V_N where N is equal or larger than 20 vacancies.

Note that positrons can be also trapped at <100> edge and ½ <111> screw dislocations as it has been calculated for iron and tungsten [43] and observed in iron [44] and in tungsten [45]. The specific annihilation characteristics S_j, W_j of this type of defects have not yet been determined in tungsten. Only the calculated positron lifetimes can be found in literature [43,46]. Depending on the nature of a dislocation, the lifetime varies generally between a value close to the lifetime in the perfect lattice (τ_L =101 ps in tungsten) [39] and the one in a single vacancy (τ_V =193 ps in tungsten) [35] due to the fact that open volume is lower in the core of a dislocation than in a vacancy. The positron lifetime in the core of ½ <111> screw and <100> edge dislocations has been calculated as 130 ps and 161 ps, respectively [43]. When vacancies are bound to the dislocation line, the lifetime increases and reaches a value close to the lifetime of a positron in a bound vacancy cluster. The same trends have been found in iron [43]. Recently the values of S_{dis} and W_{dis} specific to dislocations have been determined for iron [47]. As expected, the characteristic $\left| (S_{dis} - S_L)/(W_{dis} - W_L) \right|$ ratio is lower than the same ratio for a single

vacancy V $\left|(S_V\text{-}S_L)/(W_V\text{-}W_L)\right|$. The same relationship is also expected for the bcc tungsten. The trapping coefficient of positrons at a dislocation μ_{disl} is not known for tungsten.

3.2 Unirradiated samples results

The *S(E)* and *W(E)* curves measured in unirradiated tungsten sample are plotted in Figure 8. These experimental data can be fitted with the VEPFIT program, considering the sample as one homogeneous layer. The results are reported in Table 3. The line-shape parameters for unirradiated sample are S_{unirr} = 0.370(1), W_{unirr} = 0.083(1). These values are respectively slightly higher and lower than the perfect lattice parameters S_L and W_L. This indicates that some of the positrons annihilate while trapped in vacancy defects, but the concentration of these defects remains low. This is also confirmed by the high value of the effective diffusion length of 80±1 nm which appears to be very close to the values available in literature for perfect crystalline tungsten [37,41], namely 80–135 nm. This indicates that the concentration of defects in the bulk of un-irradiated sample is low, and lower than 10^{24} m^{-3}.

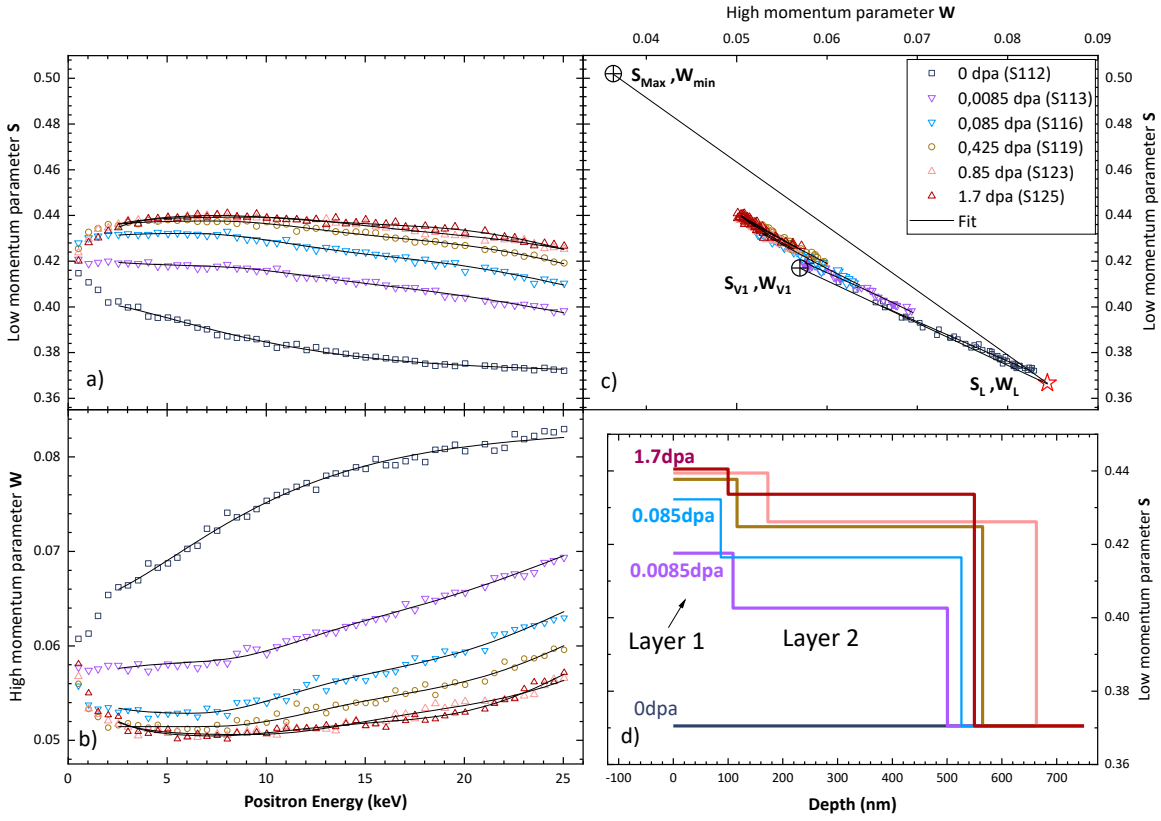

Figure 8. Evolution of the positron annihilation characteristics in unirradiated tungsten sample and in samples after irradiation to doses between 0.0085 and 1.7 dpa. (a) Low momentum fraction *S*, and (b) high momentum fraction *W* as functions of the positron energy. (c) *W* plotted as a function of *S*. The *S*, *W* values for the annihilation in lattice (S_L, W_L), single vacancy (S_{V1}, W_{V1}), and maximum *S* and minimum *W* are also plotted (S_{Max}, W_{Max}). The experimental data

are plotted in open symbols and the fitted curves are given in continuous line. (d) the *S(z)* and *W(z)* depth profiles extracted from *S(E)* and *W(E)* using VEPFIT (see details in the text).

3.3. Irradiated samples results

Line-shape parameters *S(E)* and *W(E)* measured after irradiation with 2 MeV tungsten ions at various fluences are plotted in Figure 8. With increasing irradiation dose, the *S* and *W* values drastically increase and decrease, respectively. This indicates that positrons respond to the presence of defects generated during implantation for all the fluences studied.

For the sample irradiated at the lowest dpa level (0.0085 dpa), *S* remains constant in the energy range between 0.5 and 8 keV and then decreases slowly. This indicates that the damage level decreases when the depth increases, in agreement with SRIM calculations. The $\left|(S-S_L)/(W-W_L)\right|$ ratio for the plateau values (1.96(4)) is higher than the one for the single vacancy (1.85(3)) indicating that vacancy clusters are detected. These clusters are probably formed in collision cascades. Fitting of *S(E)* and *W(E)* with the VEPFIT program requires a model with a minimum of 3 homogeneous layers to correctly describe the experimental curves. Models with 3 and 4 layers have been tested. The one with 3 layers has been chosen because the number of parameters is minimized, and the quality of the fit is acceptable (as seen in Figure 8). In these fits the annihilation characteristics of the last layer, which is not damaged, have been fixed at values $S_{Lay}(3)$ = 0.370, $W_{Lay}(3)$ = 0.083 and the effective diffusion length $L_{Lay}(3)$ was taken to be 80 nm in agreement with the values obtained for the bulk of unirradiated samples. The annihilation characteristics extracted for layers 1 and 2, S_{Lay}, W_{Lay}, and L_{Lay} are reported in Table 3 with the annihilation characteristics S_{Surf} and W_{Surf} at the surface of the samples. The thickness of the first layer is about 100 nm for the irradiated samples with damage dose lower or equal to 0.425 dpa. This value is close to the depth of maximal damage at the maximum dpa level calculated using SRIM (see Figure 7). When the dpa level becomes equal or larger than 0.85 dpa, the thickness of the first layer increases to about 170 nm. The $S_{Lay}(1)$, $W_{Lay}(1)$ values extracted from the fitting correspond to the maximum damage induced for each damage dose. Note that these values represent the mean of *S(E)* and *W(E)* calculated in the energy range between 7 and 8.5 keV.

		Damage dose (dpa)				
		0.0085	0.085	0.425	0.85	1.7
	S_{Surf}	0.419(1)	0.430(1)	0.432(1)	0.431(1)	0.431(1)

Surface	W_{Surf}	0.057(1)	0.054(1)	0.053(1)	0.054(1)	0.054(1)
Layer 1	S_{Lay}	0.418(1)	0.432(1)	0.438(1)	0.440(1)	0.440(1)
	W_{Lay}	0.058(1)	0.053(1)	0.051(1)	0.050(1)	0.050(1)
	$(S_{Lay}\_S_L)/(W_{Lay}-W_L)$	1.96(4)	2.10(4)	2.15(4)	2.15(4)	2.15(4)
	$L^+_{Lay\ (nm)}$	14(4)	4-6	4-5	5-7	5-7
	Thickness (nm)	100(5)	90(5)	110(10)	120-170	120-170
Layer 2	S_{Lay}	0.402(1)	0.417(1)	0.425(1)	0.428(5)	0.428(5)
	W_{Lay}	0.067(1)	0.059(1)	0.057(1)	0.054(2)	0.054(2)
	$L^+_{Lay\ (nm)}$	60	50	45	30	30
	Thickness (nm)	510(10)	510(20)	570(10)	610(45)	610(45)
Vacancy concentration (m^{-3})		9.2×10^{25}				
Mean defect size by TEM (nm)					3.4±0.1	
Mean defect volume density by TEM (loops/m^2)					$(3.94\pm0.1)\times10^{13}$	

Table 3. Annihilation characteristics S_{Surf} *and* S_{Surf} for surface, $S_{Lay}(i)$, $W_{Lay}(i)$**,** and $L_{Lay}(i)$ for layers i = 1,2, extracted from fitting of the *S(E)* and *W(E)* curves with the VEPFIT program using a three layers model for irradiated samples at different damage doses between 0.0085 and 1.7 dpa.

$S_{Lay}(1)$ increases and $W_{Lay}(1)$ decreases first rapidly when damage dose reaches 0.085 dpa and then more slowly to 0.85 dpa. Then, they remain constant when damage dose is increased again by a factor of 2. The saturation values of $S_{Lay}(1)$ and $W_{Lay}(1)$ are $S_{Sat}(1)$ = 0.440(1) and $W_{Sat}(1)$ = 0.050(1). Note that they are the same as the values obtained for damage dose of 1 dpa and also 12 dpa using other irradiation conditions (20 MeV W^+ ions at room temperature [48]). The $S_{Lay}(1)/S_L$ normalized values measured in the irradiated samples are plotted as a function of dpa level in Figure 9.

The effective diffusion length L_{Lay} (1), is 14(4) nm after irradiation at the lowest damage dose. It is much lower than in the virgin sample (80(1) nm) indicating a high positrons trapping rate at defects. L_{Lay} (1) decreases to a very low value of 4-6 nm when irradiation fluence increases indicating that the concentration of defects increases. Finally, L_{Lay} (1) remains constant for high damage dose equal or higher than 0.085 dpa.

The $\left|(S_{Lay}(1)-S_L)/(W_{Lay}(1)-W_L)\right|$ ratio also increases slightly when the dose increases up to 0.425 dpa, indicating that the proportion of the largest vacancy clusters increases with the damage dose probably because of the overlap of collision cascades. As the values of $S_{Lay}(1)$ and $W_{Lay}(1)$ and L_{Lay} (1), this ratio doesn't change for the highest damage doses larger or equal

than 0.85 dpa. Overall, PAS results detect a saturation when the dpa level becomes higher than 0.425 dpa indicating that the types of vacancy defects detected no more change. Such saturation can be due to either the saturation of the induced damage or to the saturation of positron trapping at the detected type of defects and no change in the annihilation characteristics can be observed. This point will be discussed in Section 4. Similar saturation in tungsten has been observed by Ogorodnikova and Gann [49] when studying deuterium concentration after irradiation with 20 MeV W ions, with saturation dose of ~0.45 dpa, very close to 0.425 dpa in the present study. The effect of saturation was also found in Eurofer steel at 0.25 dpa [50], while another study [15] found rapid saturation (below 0.1 dpa) in Fe-Cr alloy but decrease of overall deuterium concentration in Eurofer at 1 dpa compared to 0.1 dpa. It can be added that if the concentration of defects would increase with damage dose the PAS results show that the proportion of the different defects does not change.

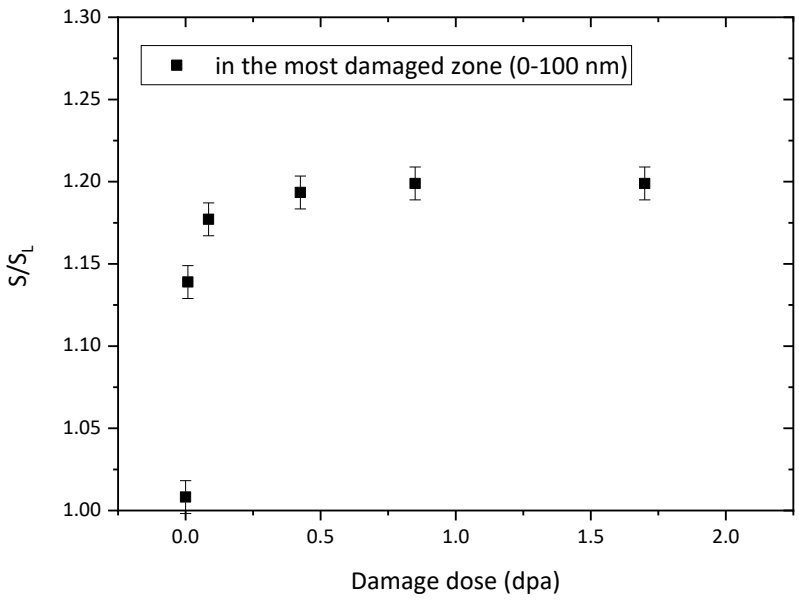

Figure 9. Low momentum annihilation fraction in the most damaged zone as a function of dpa level in self irradiated (2 MeV W^+ ions) tungsten samples.

4. Discussion

We have seen above that the *S* and *W* values obtained in the most damaged zone of self-irradiated tungsten samples vary with damage dose. The *S*, *W* values in the sample irradiated

at the lowest damage dose (0.0085 dpa) are very close to the annihilation characteristics of a single vacancy suggesting that single vacancies represent the majority of vacancy type defects. The concentration of these individual vacancies C_V can be estimated from the effective diffusion length using a one trap trapping model where positrons can annihilate in only one type of defect, a single vacancy. C_V can be extracted from (1) where K_j with $j > 1$ is equal to 0 as it has been done already for Ni containing a high concentration of defects [51]. Thus C_V can be written as follows:

$$C_V = {\lambda_L}/{\mu_V}\left[\left({L^+}/{L_{eff}^+}\right)^2 - 1\right] \quad (4)$$

where L_{eff}^+ is the effective diffusion length in the damaged layer, L^+ is the intrinsic positron diffusion length (80-135 nm), λ_L the lattice annihilation rate ($\lambda_L = 1/\tau_L$), and μ_V the trapping coefficient of a positron at a single vacancy.

For the lowest damage dose, L_{eff}^+ has been found to be equal to 14(4) nm (see Table 3) and the corresponding vacancy concentration has the mean value of 9.2×10^{25} m^{-3}. As the damage dose increases, we observe that L_{eff}^+ decreases and that the $\left|(S_{Lay}(1)-S_L)/(W_{Lay}(1)-W_L)\right|$ ratio increases, indicating that positron trapping increases and that vacancy clusters are detected. The one trap trapping model can no longer be used, and the values of *S* and *W* become the results of annihilation of positrons trapped in a variety of vacancy defects, single vacancies, vacancy clusters and possibly at some dislocation type defects. TEM results presented in Section 2.2 showed that dislocation loops are generated in self-irradiated samples as it was already observed in literature (see [52], for example). Their density per unit area is estimated to be $(3.94\pm0.1)\times10^{13}$ loops/m² at 0.85 dpa. If we consider that the thickness of the sample is in the range from 50 to 150 nm (to ensure that the sample is transparent to 200 keV electrons) the loops volume density can be estimated to be in the range from $3\text{-}8\times10^{20}$ m^{-3}. We note that this density was evaluated using only one diffraction vector **g** =<110>. If we assume that both families of <100> and ½ <111> loops are generated in the same proportion during irradiation, we estimate from the invisibility rules that only 60% of the dislocation loops are detected. As showed in [45], the fraction of the <100> loops is expected to be lower than the ½<111> loops. If we consider, as the worst-case scenario, that no <100> loops are created, only 50% of loops are detected in the observation conditions used in this study. Even if we take into account that not all the dislocation loops are detected, their concentration remains low and at most can be twice the one measured in TEM micrographs, meaning that it is in the range from $0.6\text{-}1.6\times10^{21}$

m^{-3} for 0.85 dpa. At this damage dose the fraction of positrons that could be trapped at dislocation loops is negligible and positron annihilation characteristics are only representative of vacancy defects, including single vacancies and vacancy clusters V_n.

The value of the $|(S_{Lay}(1)-S_L)/(W_{Lay}(1)-W_L)|$ ratio in the damaged layer reaches 2.15 at the maximum when the damage dose becomes equal or higher than 0.425 dpa. This value corresponds to an intermediate value between the V_N related ratio ($|(S_{max}-S_L)/(W_{min}-W_L)| = 2.8$) and the single vacancy one ($|(S_V-S_L)/(W_V-W_L)| = 1.8$). It suggests that vacancy clusters V_n detected in the damaged layer are small and n is probably not larger than 5-7. When the dose becomes larger than 0.0085 dpa, positrons annihilate in single vacancy defects and in vacancy clusters V_n where n varies from 2 to 5-7. The concentration of each type of defect cannot be determined because not only are the specific values S_{Vn}, W_{Vn} of vacancy clusters V_n are not known but also because their corresponding annihilation fractions cannot be extracted. Nevertheless the total positron trapping rate K_{tot} can be written as the sum of the trapping rate in single vacancies and the trapping rate in each type of vacancy clusters: $K_{tot} = K_V + \sum_{n=2}^{5-7} K_{V_n}$. The concentration of each type of defect cannot be determined because not only are the S_{Vi}, W_{Vi} of vacancy clusters not known, but also because their corresponding annihilation fractions cannot be extracted. It is however possible to extract from the effective diffusion length L_{eff}^{+} obtained in the damaged layer the total vacancy defects concentration. Indeed, L_{eff}^{+} can be written as follows:

$$L_{eff}^{+} = \sqrt{\frac{D_+}{\lambda_L + K_V + \sum_{N=2}^{5-7} K_{V_n}}} \tag{5}$$

where K_V and K_{V_n} are the positron trapping rates at the single vacancy and the vacancy clusters V_n, respectively. For L_{eff}^{+} = 4 nm (see Table 3), $K_V + \sum_{N=2}^{5-7} K_{V_n} = 7.2\times10^{12}$ s^{-1}. K_V is the product of the trapping coefficient μ_V by the vacancy concentration C_V and $K_{V_n} = \mu_{V_n} \times C_{V_n}$ and $\mu_{V_n} = n \times \mu_V$. It follows that the total vacancy defect concentration C_V^{tot}, which is the sum of the concentration of isolated vacancies and concentration of vacancy clusters, can be estimated from equation

$$C_V^{tot} = C_V + \sum_{n=2}^{5-7} nC_{V_n} = \frac{K_{tot}}{\mu_V}. \tag{6}$$

K_{tot} could be estimated from the value of the effective diffusion length as it has been done just above for the lowest damage dose. However, the extraction of the effective diffusion length

becomes difficult for damage dose higher than 0.0085 dpa. The obtained values range between 4 and 7 nm and depends strongly to the annihilation characteristics of the second layer, in particular its thickness and the effective diffusion length. The concentration of vacancy defects cannot be determined, and it is possible to estimate a lower limit of C_V^{tot} assuming that the effective diffusion length is equal to 6 nm. In this case, C_V^{tot} would be higher or about 5×10^{26} m^{-3} for damage dose of 0.085 dpa. From 0.425 dpa, we have seen in section 3.3 that PAS results detect a saturation when the dpa level increases indicating that the types of vacancy defects detected no more change. Such saturation can be due to either the saturation of the induced damage or to the saturation of positron trapping at the detected type of defects. The values of $S_{Lay}(1)$ and $W_{Lay}(1)$ and L_{Lay} (1), and the $\left|(S_{Lay}(1)-S_L)/(W_{Lay}(1)-W_L)\right|$ ratio don't change for the highest damage doses larger or equal than 0.85 dpa indicating that if the concentration of defect would increases with damage dose the proportion of each would not evolve indicating a saturation state in the defects size distribution. Moreover, it can be observed that the thickness of the highest damage region (layer 1) increases when damage dose increases above 0.425 dpa and changes from approximately 100 nm for the lowest dpa levels to up to 170 nm for the highest ones. These results can be compared to the TDS inventory data, where overall deuterium content was found to be close for the S40 sample irradiated at 0.1 dpa (4.408×10^{19} atoms/m^2) and for the S41 sample irradiated at 0.85 dpa (3.564×10^{19} atoms/m^2). It is known that hydrogen isotopes trapping (the number of atoms in each defect type) depends on defect nature. From PAS we know that the change in the size distribution of vacancy defects is low between these two damage doses. The $\left|(S_{Lay}(1)-S_L)/(W_{Lay}(1)-W_L)\right|$ ratio is 2.10(4) for 0.085 dpa and reaches the saturation value of 2.15(4). It follows that the change in concentration of vacancy defects should be also low if we consider the H release which is even lower for the highest damage dose. It suggests that the concentration of vacancy defects reaches a saturation when irradiation induced damage becomes higher than 0.5 dpa.

A similar trend, indicating that the vacancy content in crystalline tungsten exposed to irradiation increases as a function of dose and reaches saturation at a dose above approximately 0.5 dpa, was also found in direct atomistic simulations of highly irradiated tungsten and iron performed using the creation-relaxation algorithm [53]. This simulation approach assumes a uniform spatial probability distribution of generation of defects, where at each step of execution of the algorithm, a randomly chosen atom is displaced to a random location within the simulation cell. Upon creation of a Frenkel pair, conjugate gradient minimization of the resulting atomic structure is employed to relax the position of all the atoms towards a local

potential energy minimum. The subsequent events of creation and relaxation of defect structures gradually generate microstructures whose statistical descriptors do not change with respect to further irradiation, showing no further increase of defect content as a function of dose. The dose itself, expressed in terms of the canonical dpa parameter, is defined as the ratio of the total number of Frenkel pairs created from the start of the simulation to the total number of atoms in the simulation cell. A detailed discussion of the relation between the measure of radiation exposure (dpa), related to the rate of defect production by impacts of energetic particles, and the cdpa parameter used in CRA simulations, is given in Ref. [54]. While the cdpa provides a mechanistic measure of generation of defects, applicable to a material with any structure, other measures of exposure to irradiation typically involve steps where the energy of an impact is converted into the number of defects that the impact event is expected to produce. Establishing a connection between the two parameters, cdpa and NRT dpa, involves the evaluation of the slope of a curve describing how the concentration of defects varies with the dose in the infinitely small dose limit. The corresponding procedure is illustrated in Figure 1 of Ref. [54], where an explicit link between the dpa and cdpa parameters is established.

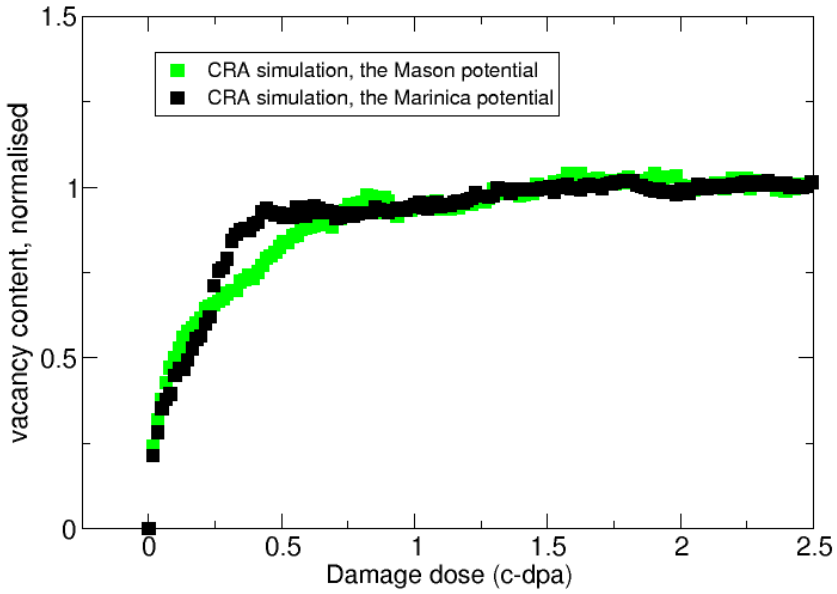

Figure 10. Variation of vacancy content in tungsten as a function of canonical dpa (c-dpa) predicted by simulations performed using the creation-relaxation algorithm (CRA) for two different interatomic potentials [53]. The values are normalised to the asymptotic high dose vacancy content, which for the Marinica potential [55] is close to 5% and for the Mason potential [56] is close to 2%.

The simulations, illustrated in Figure 10, show that after a brief period of linear accumulation that ends at ~ 0.02 dpa, the vacancy content gradually saturates as a result of build-up of internal spatially fluctuating microscopic stress caused by the defects. Similarly to the experimental curve shown in Figure 9, saturation is predicted to occur at the dose close to 0.5 dpa. Simulations also show that the density of dislocation loops in the limit of high dose is relatively low, since the majority of self-interstitial defects are now incorporated into an extended dislocation network and hence become no longer detectable by transmission electron microscopy in the form of isolated individual dislocation loops. The creation-relaxation algorithm generates microstructures that evolve solely by the relaxation of stress produced by the events of formation of Frenkel pairs, and involves no thermally activated processes. The observed saturation is the result of accumulation of high concentration of vacancies, leading to a dynamic equilibrium between the generation and annihilation of defects. Simulations show that dynamic saturation occurs at ~ 0.1 dpa [53], similar to what is found in direct cascade overlap simulations [57,58]. The validity of the pattern of microstructural evolution in tungsten derived from creation-relaxation algorithm simulations is confirmed by the observation of variation of lattice strain as a function of exposure to irradiation [59]. The origin of saturation, while related to the overlap between the spatial regions affected by collision cascades [49], is fundamentally related to the evolution of defect microstructure and occurs at a significantly higher exposure to ion irradiation than the dose of ~0.01 dpa characterising the onset of spatial overlap between the subsequent cascade events [21].

The creation-relaxation algorithm [53] simulates microstructural evolution driven by local stress and not by thermal fluctuations, and as a result it is expected that the simulations should overestimate the absolute vacancy content [59]. However, given that in irradiated tungsten vacancies do not diffuse appreciably below 350 °C [60,61], the assumption that the thermal relaxation of defect structure is impeded and effectively does not occur at room temperature, is broadly justified and agrees with direct real-space electron microscope observations of thermal annealing of extended dislocation microstructure of heavily irradiated tungsten, which remains thermally stable at temperatures up to 800 °C [62].

5. Conclusions

This study shows that tungsten irradiated to high dose at relatively low temperatures close to room temperature, and below approximately 350°C, develops a characteristic microstructure

dominated by vacancy type defects. The density of self-interstitial dislocation loops is relatively low, in agreement with recent simulations [53], suggesting that self-interstitial defects tend to incorporate themselves into an extended dislocation network that readily forms in the material at doses exceeding 0.1 dpa. At the same time, isolated vacancy defects, according to predictions derived from simulations, dominate the microstructure. The saturation of damage found in PAS agrees with simulated microstructures generated using the creation-relaxation algorithm. Implications of the observed saturation for the retention of hydrogen isotopes in irradiated tungsten and other materials are profound, and will be assessed in further work involving materials exposed to higher irradiation doses, and involving other hydrogen isotopes.

Acknowledgments

Some of the research used equipment at the UKAEA's Materials Research Facility (MRF) which is part of the UK's Henry Royce Institute and National Nuclear User Facility initiatives. We thank the MRF staff for their support. This work was supported by EUROfusion Enabling Research project TRiCEM, Tritium Retention in Controlled and Evolving Microstructure. This work has been carried out within the framework of the EUROfusion Consortium and has received funding from the Euratom research and training programme 2014-2018 and 2019-2020 under Grant Agreement No. 633053. The views and opinions expressed herein do not necessarily reflect those of the European Commission. We acknowledge funding by the RCUK Energy Programme (Grant No. EP/T012250/1).

Data availability

The raw data required to reproduce these findings are available to download from https://drive.google.com/file/d/1oLWxInUPcnJZBVeP5vdKa4B8gp0gO6_X/view. The processed data required to reproduce these findings are available to download from https://drive.google.com/file/d/1oLWxInUPcnJZBVeP5vdKa4B8gp0gO6_X/view. The raw/processed data required to reproduce the TEM and PAS results cannot be shared at this time due to time limitations and specialized software required to open the raw data. Data can be made available on request by emailing Anthony.Hollingsworth@ukaea.uk.

References

[1] M. Rieth *et al.*, Advances in Science and Technology **73**, 11 (2010).
[2] T. Hirai *et al.*, Nuclear Materials and Energy **9**, 216 (2016).

[3] M. Rieth *et al.*, Journal of Nuclear Materials **432**, 482 (2013).
[4] D.T. Blagoeva *et al.*, Journal of Nuclear Materials **442**, S198 (2013).
[5] B. Lipschultz *et al.*, Massachusetts Institute of Technology Report PSFC/RR-10-4, 2010.
[6] J. Marian *et al.*, Nuclear Fusion **57**, 092008 (2017).
[7] K. Heinola *et al.*, Phys. Rev. B **82**, 094102 (2010).
[8] K. Ohsawa *et al.*, Journal of Nuclear Materials **527**, 151825 (2019).
[9] S. Nagata and K. Takahiro, Journal of Nuclear Materials **283-287**, 1038 (2000).
[10] O.V. Ogorodnikova, Journal of Nuclear Materials **390-391**, 651 (2009).
[11] V.Kh. Alimov *et al.*, Journal of Nuclear Materials **441**, 280 (2013).
[12] T. Schwarz-Selinger, Nuclear Materials and Energy **12**, 683 (2017).
[13] B. Tyburska *et al.*, Journal of Nuclear Materials **395**, 150 (2009).
[14] B. Wielunska *et al.*, Nuclear Fusion **60**, 096002 (2020).
[15] A. Hollingsworth *et al.*, Nuclear Fusion **60**, 016024 (2020).
[16] P. Hautojärvi and C. Corbel, in: Positron Spectroscopy of Solids: Proceedings of the International School of Physics 'Enrico Fermi', A. Dupasquier and A.P. Mills Jr., (Eds.), IOS Press, Amsterdam, 1995, p. 491.
[17] A. Dupasquier and G. Ottaviani, in: Positron Spectroscopy of Solids: Proceedings of the International School of Physics 'Enrico Fermi', A. Dupasquier and A.P. Mills Jr., (Eds.), IOS Press, Amsterdam, 1995, p. 581.
[18] M.-F. Barthe, EPJ Web of Conferences **115**, 03004 (2016), https://doi.org/10.1051/epjconf/201611503004
[19] X. Yi *et al.*, Europhys. Lett. **110**, 36001 (2015).
[20] J.F. Ziegler, M.D. Ziegler, and J.P. Biersack, Nuclear Instruments and Methods in Physics Research B **268**, 1818 (2010).
[21] R.E. Stoller *et al.*, Nuclear Instruments and Methods in Physics Research B **310**, 75 (2013).
[22] http://www.SRIM.org
[23] J.-P. Crocombette and C. Van Wambeke, EPJ Nuclear Sciences and Technologies **5**, 7 (2019).
[24] D.R. Mason *et al.*, Journal of Physics : Condensed Matter **26**, 375701 (2014).
[25] O.V. Ogorodnikova *et al.*, Physics Procedia **71**, 41 (2015), https://doi.org/10.1016/j.phpro.2015.08.309
[26] M.T. Robinson and I.M. Torrens, Physical Review B **9**, 5008 (1974).
[27] D.R. Mason *et al.*, Acta Materialia **144**, 905 (2018).
[28] K. Arakawa *et al.*, Nature Materials **19**, 508 (2020), https://doi.org/10.1038/s41563-019-0584-0
[29] J. Wang *et al.*, Journal of Nuclear Materials **545**, 152749 (2021).
[30] M. Zibrov *et al.*, Journal of Nuclear Materials **477**, 292 (2016).
[31] O.V. Ogorodnikova, Journal of Applied Physics **118**, 074902 (2015).
[32] S. Markelj *et al.*, Nuclear Fusion **59**, 086050 (2019).
[33] W.M. Shu, E. Wakai, and T. Yamanishi, Nuclear Fusion **47**, 201 (2007).
[34] Y. Zayachuk *et al.*, Nuclear Fusion **53**, 013013 (2013).
[35] P. Desgardin *et al.*, Materials Science Forum **363-365**, 523 (2001).
[36] A. van Veen *et al.*, AIP Conference Proceedings **218**, 171 (1990).
[37] A. Vehanen *et al.*, Physical Review B **29**, 2371 (1984).

[38] P.J. Schultz and K.G. Lynn, Reviews of Modern Physics **60**, 701 (1988).
[39] T. Troev *et al*., Nuclear Instruments and Methods in Physics Research B **267**, 535 (2009).
[40] Y. Xu *et al*., Modern Physics Letters B **17**, 147 (2003).
[41] P.E. Lhuillier *et al*., Physica Status Solidi C **6**, 2329 (2009).
[42] A. Debelle, M.-F. Barthe, and T. Sauvage, Journal of Nuclear Materials **376**, 216 (2008).
[43] P. Staikov and N. Djourelov, Physica B: Condensed Matter **413**, 59 (2013).
[44] Y.-K. Park *et al*., Phys. Rev. B **34**, 823 (1986).
[45] T.E.M. Staab *et al*., Journal of Physics : Condensed Matter **11**, 1787 (1999).
[46] E. Kuramoto *et al*., Computational Materials Science **14**, 28 (1999).
[47] W. Asplet, "Experimental study of the interaction of vacancy defects with Y, O and Ti solutes to better understand their roles in the nanoparticles formation in ODS steels", PhD thesis supervised by M.-F. Barthe, Orléans, Université d'Orléans, 2018, https://tel.archives-ouvertes.fr/tel-02395001
[48] M. Sidibe, "Study of the behaviour of tungsten under irradiation: application to fusion reactors", PhD thesis supervised by M.-F. Barthe, Orléans, Université d'Orléans, 2014, https://tel.archives-ouvertes.fr/tel-01068634
[49] O.V. Ogorodnikova and V. Gann, Journal of Nuclear Materials **460**, 60 (2015).
[50] O.V. Ogorodnikova *et al*., Nuclear Fusion **57**, 036011 (2017).
[51] R. Krause-Rehberg *et al*., Nuclear Instruments and Methods in Physics Research B **240**, 719 (2005).
[52] X. Yi *et al*., Acta Materialia **112**, 105 (2016).
[53] P.M. Derlet and S.L. Dudarev, Physical Review Materials **4**, 023605 (2020).
[54] D. R. Mason *et al*., Physical Review Materials **5**, 095403 (2021).
[55] M.-C. Marinica *et al*., Journal of Physics: Condensed Matter **25**, 395502 (2013).
[56] D.R. Mason, D. Nguyen-Manh, and C.S. Becquart, Journal of Physics : Condensed Matter **29**, 505501 (2017).
[57] F. Granberg *et al*., Physical Review Letters **116**, 135504 (2016).
[58] L. Koch *et al*., Journal of Applied Physics **122**, 105106 (2017).
[59] D. Mason *et al*., Physical Review Letters **125**, 225503 (2020).
[60] M.W. Thompson, Philosophical Magazine **5**, 278 (1960).
[61] J. Heikinheimo *et al*., APL Materials **7**, 021103 (2019)
[62] F. Ferroni *et al*., Acta Materialia **90**, 380 (2015).

Credit Author Statement

A. Hollingsworth - Conceptualization, Methodology, Validation, Formal analysis, Investigation, Resources, Data Curation, Writing - Original Draft, Writing - Review & Editing, Visualization, Supervision, Project administration, Funding acquisition

M.-F. Barthe - Conceptualization, Methodology, Validation, Formal analysis, Investigation, Data Curation, Writing - Original Draft, Visualization, Supervision

M.Yu. Lavrentiev - Conceptualization, Methodology, Validation, Writing - Original Draft, Writing - Review & Editing, Visualization

P.M. Derlet - Methodology, Software, Validation, Formal analysis, Investigation, Data Curation, Visualization

S.L. Dudarev - Conceptualization, Methodology, Software, Validation, Formal analysis, Investigation, Data Curation, Writing - Original Draft, Visualization

D.R. Mason - Methodology, Software, Validation, Formal analysis, Investigation, Data Curation, Visualization

Z. Hu - Software, Validation, Formal analysis, Investigation

P. Desgardin - Software, Validation, Formal analysis, Investigation

J. Hess - Resources

S. Davies - Validation

B. Thomas - Investigation

H. Salter - Investigation

E.F.J. Shelton - Writing - Review & Editing

K. Heinola - Methodology, Validation

K. Mizohata - Validation

A. De Backer - Conceptualization, Methodology, Software, Validation, Supervision, , Project administration, Funding acquisition

A. Baron-Wiechec - Methodology, Validation, Formal analysis, Investigation

I. Jepu - Validation, Formal analysis, Investigation, Data Curation

Y. Zayachuk - Methodology, Validation, Formal analysis, Writing - Original Draft, Visualization

A. Widdowson - Validation, Supervision

E. Meslin - Conceptualization, Methodology, Software, Validation, Formal analysis, Investigation, Resources, Data Curation, Writing - Original Draft, Visualization, Supervision

A. Morellec - Software, Validation, Formal analysis, Investigation